

SOLAR FLARE MODEL ATMOSPHERES

Suzanne L. Hawley¹

Institute of Geophysics and Planetary Physics
Lawrence Livermore National Laboratory
P.O. Box 808, Mail Code L-413
Livermore, CA 94551
email: slh@sunlight.llnl.gov

and

George H. Fisher

Space Sciences Laboratory
University of California
Berkeley, CA 94720
email: fisher@sunspot.ssl.berkeley.edu

Running page head: Solar Flare Model Atmospheres

Send proofs to:

Suzanne L. Hawley
Department of Physics and Astronomy
Michigan State University
East Lansing, MI 48824

Footnote: ¹Hubble Fellow

(NASA-CR-197607) SOLAR FLARE MODEL
ATMOSPHERES (LLNL) 59 p

N95-19034

Unclas

63/92 0038409

ABSTRACT

Solar flare model atmospheres computed under the assumption of energetic equilibrium in the chromosphere are presented. The models use a static, one-dimensional plane parallel geometry and are designed within a physically self-consistent coronal loop. Assumed flare heating mechanisms include collisions from a flux of non-thermal electrons and X-ray heating of the chromosphere by the corona. The heating by energetic electrons accounts explicitly for variations of the ionized fraction with depth in the atmosphere. X-ray heating of the chromosphere by the corona incorporates a flare loop geometry by approximating distant portions of the loop with a series of point sources, while treating the loop leg closest to the chromospheric footpoint in the plane-parallel approximation. Coronal flare heating leads to increased heat conduction, chromospheric evaporation and subsequent changes in coronal pressure; these effects are included self-consistently in the models. Cooling in the chromosphere is computed in detail for the important optically thick H I, Ca II and Mg II transitions using the non-LTE prescription in the program MULTI. Hydrogen ionization rates from X-ray photo-ionization and collisional ionization by non-thermal electrons are included explicitly in the rate equations. The models are computed in the "impulsive" and "equilibrium" limits, and in a set of intermediate "evolving" states. The impulsive atmospheres have the density distribution frozen in pre-flare configuration, while the equilibrium models assume the entire atmosphere is in hydrostatic and energetic equilibrium. The evolving atmospheres represent intermediate stages where hydrostatic equilibrium has been established in the chromosphere and corona, but the corona is not yet in energetic equilibrium with the flare heating source. Thus, for example, chromospheric evaporation is still in the process of occurring.

We have computed the chromospheric radiation that results from a range of coronal heating rates, with particular emphasis on the widely observed diagnostic $H\alpha$. Our principal results are:

- (1) Only in models with low coronal pressure (i.e. in models where very little evaporation has occurred) does the non-thermal electron flux provide significant heating in the chromosphere.
- (2) After evaporation has occurred and the coronal pressure is high, the dominant source of chromospheric heating is the X-ray irradiation from the hot corona. However, this reprocessed heat source never exceeds $\sim 6\%$ of the original flare energy flux deposited in the corona by the beam.
- (3) In order to obtain the broad, intense $H\alpha$ profiles that are actually observed in flares, there must be either (a) a condition of low coronal pressure in the overlying loop; or (b) heating at the top of the chromosphere from a source other than the beam and its products (X-rays, heat conduction). The reason is that only with a low pressure corona is there enough chromospheric heating from the beam to raise enough column mass to temperatures of $\sim 10^4\text{K}$ necessary to produce copious $H\alpha$.
- (4) The depth of the $H\alpha$ central reversal was correlated with the incident coronal beam flux F_{20} in our models in the sense that models with large beam flux have profiles with smaller central reversal.
- (5) Losses from ions other than those we treat in detail play a very important, and in many cases dominant, role in the cooling of the chromosphere. Future models should include the radiation backwarming effects of these losses.
- (6) The power law dependence of the ratio $F_{H\alpha}/F_{20}$ on the beam flux F_{20} , which has been empirically determined, was reproduced in some of our models. However, we find that a more physically meaningful parameter *during the evolution of a single loop* is the pressure, P , since the chromospheric heating after evaporation has occurred depends primarily on the coronal pressure (or alternatively the conductive flux or coronal column depth) and not on the beam flux.

Our conclusion is that the $H\alpha$ fluxes and profiles actually observed in flares can only be produced under conditions of a low pressure corona with strong beam heating. Therefore we suggest that $H\alpha$ in flares is produced primarily at the footpoints of newly

heated loops where significant evaporation has not yet occurred. As a single loop evolves in time, no matter how strong the heating rate may become, the $H\alpha$ flux will diminish as the corona becomes denser and hence more effective at stopping the beam. This prediction leads to several observable consequences regarding the spatial and temporal signatures of the X-ray and $H\alpha$ radiation during flares.

1. INTRODUCTION

The recent advent of unprecedented high resolution X-ray flare observations from space (in particular those from the Yohkoh spacecraft), combined with improved high resolution optical observations from several ground-based observatories strongly motivate a fresh theoretical investigation of energy transport during solar flares. In this paper, we will investigate the transport of energy into the chromosphere from the corona, where flare energy release is generally believed to occur. We present here a new set of theoretical models of solar flare atmospheres that are designed to help interpret the current generation of flare observations.

Two differing approaches have been used in the past to develop theoretical models of flare atmospheres (Ricchiuzzi and Canfield 1983, henceforth RC). The “semi-empirical” models are generated by iteratively guessing the temperature and density structure in the atmosphere, solving the statistical equilibrium and radiation transport equations, and then comparing computed diagnostics with flare observations. Recent examples of such models include those of Machado *et al* (1980); Avrett, Machado and Kurucz (1986), and Mauas, Machado and Avrett (1990). Although semi-empirical models are relatively straightforward to generate, the models are not related *a priori* to any particular model of flare energy transport, and are thus difficult to interpret. The second approach to computing flare atmospheres, dubbed the “synthetic” approach by RC, consists of specifying the form of an atmospheric heating function to be identified with a particular model of flare heating. In these models, the energy equation, the radiation transport equation, and the statistical equilibrium equations are solved simultaneously, so that the temperature, density, level populations, and radiation fields are computed self-consistently from the proposed flare heating mechanism. By studying changes in

computed radiation fields with changes in parameters that describe flare heating, diagnostics can be developed to compare with observations. Synthetic models are thus more useful in interpreting flare observations, but are generally far more difficult to generate than semi-empirical models. The only presently existing set of synthetic models of the solar flare chromosphere are those of RC and Canfield, Gunkler and Ricchiazzi (1983, henceforth CGR).

The RC and CGR model atmospheres, however, contain several defects which limit their usefulness. First, the treatment of the radiation transport equations in all the transitions considered is via the approximate, frequency-integrated “probabilistic” equations (Canfield, McClymont and Puetter 1983; Canfield and Ricchiazzi 1980) rather than the exact, frequency dependent equations. A serious shortcoming of the probabilistic method is that backheating of the lower chromosphere and temperature minimum region by the upper chromosphere is neglected. The importance of backheating in the temperature minimum region during flares has recently been demonstrated by Metcalf, Canfield and Saba (1990). They find that backheating by bound-free continuum radiation emitted from the upper flare chromosphere is the best explanation of temperature minimum heating in the flares that they observed. It is thus essential that theoretical models of the flare chromosphere incorporate the exact radiation transport equations, in order to include backheating. A second difficulty is that RC used only a 2-level plus continuum hydrogen atom. Gayley (1990) has shown that the inclusion of at least 4 levels is necessary to get the correct ionized fraction at mid-chromospheric levels. A third defect of RC’s treatment is their parameterization of the corona. RC assumed that the effects of the corona on the lower transition region and chromosphere could be described by 2 independent parameters, P_0 (the “coronal” pressure) and F_5 (the conductive flux at $T = 10^5 K$). However, a self-consistent examination of energy balance and hydrostatic equilibrium in a flare loop reveals that P_0 and F_5 are *not* independent

parameters, but in fact should be roughly proportional to one another. Furthermore, the stated values of P_0 in their models do not necessarily coincide with the overlying coronal pressure, due to large transition region column depths in some of their models. Therefore, the RC study of the effects of coronal pressure and conductive flux on the structure of the flare chromosphere is contaminated by this hidden inter-dependence of the parameters; our new models remove this problem and allow a more quantitative comparison between theory and observations.

We have previously developed a set of synthetic models to study the flare atmosphere of the dMe star AD Leonis (Hawley and Fisher 1992, henceforth HF92). These models incorporated an overlying coronal loop structure which affected the flare chromosphere through an enhanced coronal pressure and conductive flux, as well as substantial chromospheric heating from coronal X-rays emitted in the plane parallel approximation. We now apply the same techniques, with some improvements, to the solar case. In the present work, we present a set of synthetic models of solar flare chromospheres that correct known defects and shortcomings of the RC models, and add several new important features. Our set of models covers a wide range of values for the parameters that describe flare heating by a flux of non-thermal electrons and by the radiation and conduction from the flare corona. We have improved the X-ray irradiation treatment of HF92 by including the effects of loop geometry in computing the X-ray flux incident at a loop footprint. The associated photo-ionization and non-thermal collisional ionization rates from these heating mechanisms are explicitly included in the statistical equilibrium equations. We solve the full angle and frequency dependent radiation transport equations for the important optically thick cooling transitions of H I, Ca II and Mg II using the non-LTE radiative transfer package MULTI (Carlsson 1986, Scharmer and Carlsson 1985). Other important optically thick radiative processes are included in MULTI via the LINEAR detailed description of background opacity sources (Auer,

Heasley and Mihalas 1972). Cooling at high chromospheric temperatures from ions not treated in detail is included via an “effectively thin” approximation. We insure that the coronal model specified by the heating parameters is physically consistent with our chromospheric models.

It is well known that intense heating of the atmosphere during flares drives substantial mass motions in both the corona and chromosphere, meaning that a complete characterization of the flaring atmosphere must include a description of the velocity field. However, in this paper we will focus on 3 limiting cases where a static atmosphere should be an adequate approximation to the flaring atmosphere. First, in the “Impulsive” models, applicable early in a burst of energy release, the density distribution is assumed to remain frozen in its preflare configuration, while the chromospheric temperature rises until an energy balance is achieved between flare heating and radiative cooling. Second, in the opposite limit, we identify the “Equilibrium” atmospheres, resulting after a given level of flare heating has been maintained indefinitely, and the entire atmosphere is in energetic and hydrostatic equilibrium. Finally, we introduce the intermediate “Evolving” model atmospheres, which occur after hydrostatic equilibrium in the chromosphere and corona has been established, but before energetic equilibrium in the corona has occurred. Because of the short cooling time scales in the flare chromosphere, we assume energy balance in the chromosphere has been established in all 3 sets of models. The evolving chromospheric models are closely related to our earlier work on coronal loop evolution during flares (Fisher and Hawley 1990, henceforth FH90) and provide us a way to combine observations that reflect the heating rate (*e.g.* hard X-rays) with observations of the atmospheric response to that heating (*e.g.* soft X-rays from the corona and $H\alpha$ line emission from the chromosphere). Using an observationally inferred heating rate, an appropriate loop evolution model describing the coronal response can

be used to generate the coronal conditions for the evolving chromospheric models that can then be compared with observations during the flare evolution.

The remainder of this paper is organized as follows: In §2 we present the methods we have developed for computing synthetic models and their implementation, with frequent reference to RC and our previous work in HF92. In §3 we discuss the model atmospheres we have computed, while §4 contains the detailed line profiles and line fluxes necessary for comparison to previous models and to recent observations. In §5 we summarize our work and speculate on the nature of flare energy transport implied by our results.

2. CONSTRUCTING THE MODELS

In HF92 we computed a sequence of atmospheric models designed to reproduce various levels of flare heating on a dwarf M star. In these models, an equilibrium coronal loop with apex to footpoint length L and apex temperature T_A was attached to a chromosphere and transition region model of the flare atmosphere. The entire model was assumed to be in hydrostatic equilibrium, with the transition region structure computed assuming a balance between optically thin cooling and conductive heating, while the chromospheric temperature structure was computed assuming energy balance between X-ray heating from the flare corona and radiative cooling. The total contribution to the cooling was computed by solving the radiation transport and statistical equilibrium equations for a 6 level plus continuum HI atom, a 3 level plus continuum MgII ion, and a 5 level plus continuum CaII ion, and included losses from both line and continuum contributions. Losses from other ions were included using an “effectively thin” approximation, estimated by subtracting the species we treat in detail from the Raymond,

Cox and Smith (1976) optically thin loss rate. Shortcomings of HF92 included a plane-parallel treatment of the X-ray irradiation from the corona and a neglect of other flare heating mechanisms.

In the models presented here, we have improved the realism of our calculations over those of HF92 in several ways. First, we now use a combination of plane-parallel and point source approximations (cf. Gan and Fang 1990) to compute the X-ray irradiation of the lower part of the atmosphere from a coronal loop geometry. This is described in §2.1. Second, we now include an additional source of flare heating due to Coulomb collisions from an assumed flux of non-thermal electrons; this is discussed in §2.2. In §2.3, we describe the preflare model which is used as a starting point for all the subsequent flaring atmospheric models.

2.1 X-ray Heating

We assume that the coronal loop temperature structure is determined as described in HF92, given a loop with apex to footpoint length L and coronal apex temperature T_A , that is:

$$I_x\left(\frac{11/4 - \alpha/2}{2 - \alpha}, 1/2\right) = z/L, \quad (2.1)$$

where $x \equiv (T/T_A)^{2-\alpha}$, T is the temperature within the loop, z is the distance along the loop measured from its base, $\Lambda(T) = AT^\alpha$ is the optically thin cooling function for plasma at coronal temperatures, and $I_x(a, b)$ is the normalized incomplete beta function. We assume $\alpha = -1/2$ in equation 2.1, although a more detailed characterization of the losses is used to describe the radiation emitted by the loop. To compute the approximate wavelength dependence of the X-rays emitted from the corona, we have summed the detailed emissivities of Raymond and Smith (1977) into 7 wavelength bands; these emissivities are evaluated in steps of 0.2 in $\log T$ (throughout this paper we will use \log to mean the base 10 logarithm). The breakdown of the wavelength bands, plus

the emissivities within each temperature bin, are summarized in Table 1 of HF92. To account for the effects of temperature variation along the loop on the emitted X-ray spectrum, we note that the power in a given X-ray wavelength band from a section of the loop spanning a range in $\log T$ of $\delta \log T$ ($= 0.2$ here) is given approximately by

$$P_\lambda \simeq n_e n_h \epsilon_\lambda(T) \left| \frac{dz}{d \log T} \right| A \delta \log T, \quad (2.2)$$

where $A = (\pi/4) d^2$ is the cross-sectional area of the loop, $\epsilon_\lambda(T)$ is the temperature-dependent part of the emissivity in the given temperature and wavelength range (*e.g.* from Table 1 of HF92),

$$n_e = (1 + \bar{z}Y)n_h, \quad (2.3)$$

with $\bar{z} = 2$ being the number of electrons contributed per helium atom, Y the fractional helium abundance, and n_h the hydrogen nucleus number density. From equation (2.1) and the equation of state $P = 2n_h k_b T [1 + (1 + \bar{z})/2]$, where k_b is Boltzman's constant, one can show that the quantity $|dz/d \log T|$ appearing in equation 2.2 is given by

$$\left| \frac{dz}{d \log T} \right| = \frac{(2 - \alpha)}{B \left(\frac{11/4 - \alpha/2}{2 - \alpha}, \frac{1}{2} \right)} \ln(10) L \left(\frac{T}{T_A} \right)^{11/4 - \alpha/2} \left(1 - (T/T_A)^{2 - \alpha} \right)^{-1/2}. \quad (2.4)$$

To determine the effects of X-rays emitted from the corona on the footpoint of a loop, we follow Gan and Fang (1990) and approximate distant portions of the loop by a series of point sources, while the part of the loop just above the footpoint is treated in a plane-parallel fashion. For the portions of the loop treated in the point approximation, the power $P_\lambda(T)$ computed from each temperature bin (equation 2.2) is assumed to be located at a single point coinciding with the centroid of emission. The energy flux F_λ at the top of the footpoint from each individual temperature bin is then given by

$$F_\lambda = \frac{P_\lambda(T) \cos(\theta)}{4\pi z'^2}, \quad (2.5)$$

where θ is the angle between the vertical direction and the ray connecting the footpoint and the point source, and z' is the distance between the two points (see Figure 1). The distance $z' = 2H \sin(\theta)$, where $H = 2L/\pi$ is the radius of the coronal loop arc. In terms of the distance z measured along the coronal loop arc from the footpoint, the angle $\theta = \pi z/(4L)$. The total contribution to the X-ray flux at the footpoint from all the point sources as a function of optical depth τ_λ is then given by

$$F_\lambda(\tau_\lambda) = \sum_i \frac{P_\lambda(T_i) \cos(\theta_i)}{4\pi z_i'^2} \exp[-\tau_\lambda / \cos(\theta_i)], \quad (2.6)$$

where subscript λ denotes the X-ray wavelength band under consideration, and summation occurs over temperature bins from both sides of the loop (the temperature structure is assumed to be symmetric about the apex). The point source approximations are used for all those temperature bins located a loop arc-length distance z greater than $d/4$ above the footpoint transition region, where d is the loop cross-sectional diameter.

The portion of the corona closer than $z = d/4$ to the top of the footpoint is treated in the plane parallel approximation (a discussion of why this distance is appropriate for switching between the plane parallel and point source approximations can be found in Gan and Fang [1990]). Defining the specific intensity in the vertical direction to be

$$I_\lambda^0 = \sum_i \frac{P_\lambda(T_i)}{4\pi A}, \quad (2.7)$$

where $P_\lambda(T_i)$ is from equation 2.1, summation is over those temperature bins closer than $d/4$ to the top of the footpoint, and as before $A = \pi d^2/4$ is the loop cross-sectional area (note that the factor of A cancels with the same factor in the expression 2.2 for P_λ). This expression corrects equation (8) in HF92, in which the factor of 4π in the denominator was omitted. The flux from the plane parallel contribution at depth τ_λ is then given by

$$F_\lambda(\tau_\lambda) = 2\pi I_\lambda^0 E_2(\tau_\lambda). \quad (2.8)$$

The total X-ray flux at any depth is then the sum of contributions from equations (2.6) and (2.8). In practice, we find that the plane parallel contributions are much greater than those from the point sources. Once the X-ray fluxes are known, heating and photo-ionization of hydrogen is computed as described in HF92.

2.2 Heating by Energetic Electrons

In our atmospheric models, we assume that a flux F_{20} of non-thermal electrons above a cutoff energy of $E_c = 20$ keV is injected at the top of the loop and heats the atmosphere by means of Coulomb collisions (see *e.g.* Brown 1971 or Emslie 1978). The distribution function of the injected electrons with energy E greater than E_c is assumed to vary as $(E/E_c)^{-\delta}$, where δ is referred to as the “electron spectral index”. The energetic electrons must first penetrate through the fully ionized corona, and will thereafter propagate into the chromosphere, where the ionized fraction will in general be a function of depth. Because previous treatments of partial ionization have assumed the ionized fraction is uniform in the atmosphere, we first describe in §2.2.1 our approximate method of computing the heating rate in an atmosphere with a varying ionized fraction. Next, we note that the heat deposited by the beam above the flare transition region will increase the coronal conductive flux and drive further chromospheric evaporation, increasing yet further the amount of coronal plasma through which the beam must eventually propagate. For the equilibrium and evolving models, we must therefore provide a self-consistent estimate for the equilibrium coronal column depth consistent with a given beam flux, in order to correctly calculate the effects of beam heating in the chromosphere. This calculation is described in §2.2.2.

2.2.1 Collisional Beam Heating in a Combined Coronal and Chromospheric Atmosphere

Emslie (1978) derived the collisional beam heating rate for a plasma with an arbitrary but *uniform* level of the ionized fraction. The heating rate per hydrogen nucleus in cgs units is given in that case (after correcting a few typographical errors) by

$$Q(N) = \frac{1}{2} \frac{K\gamma(\delta-2)}{\mu_0} B_{x_c} [\delta/2, 2/(4+\beta)] \frac{F_{20}}{E_c^2} (N/N_c)^{-\delta/2}, \quad (2.9)$$

where $K = 2\pi e^4$, $\beta \equiv [2x\Lambda + (1-x)\Lambda''] / [\Lambda' + x(\Lambda - \Lambda')]$, $\gamma \equiv x\Lambda + (1-x)\Lambda'$, x is the ionized fraction of hydrogen, Λ represents the Coulomb logarithm for collisions in an ionized plasma, and Λ' and Λ'' represent effective Coulomb logarithms for collisional processes with neutrals. The expression for β in Emslie (1978) contains an error which is corrected in Emslie (1981); the corrected expression is used here. Expressions for Λ , Λ' , and Λ'' are taken from Ricchiazzi (1982): $\Lambda = 65.1 + 1.5 \ln(E) - 0.5 \ln(n_h)$; $\Lambda' = 25.1 + \ln(E)$; and $\Lambda'' = 12.3 + 0.5 \ln(E)$, where E is the electron energy expressed in ergs. Assuming a spectral index of $\delta = 5$ and a 20 keV cutoff, we find an average injected electron energy of 27.6 keV, from which we compute our adopted values of $\Lambda = 24.68$ (assuming $n_h \simeq 10^{13} \text{cm}^{-3}$), $\Lambda' = 8.13$, and $\Lambda'' = 3.82$. In principle, these values should change as one moves deeper into the atmosphere and the average electron energy decreases, but since other processes are far more important, we assume the Coulomb logarithms are depth independent. The quantity $B_{x_c} [\delta/2, 2/(4+\beta)]$ represents the complete beta function if $x_c \equiv N/N_c \geq 1$, and is the un-normalized incomplete beta function if $x_c < 1$. The cutoff column depth $N_c = \mu_0 E_c^2 / [(2 + \beta/2)\gamma K]$ corresponds to the stopping depth of an electron with injection energy at the cutoff value E_c . The quantity μ_0 is the initial pitch angle of the energetic electrons.

The relative values of Λ and Λ' describe the effectiveness of stopping by the ionized and neutral components of the plasma, respectively. Thus a beam of electrons

is stopped roughly three times more effectively by the ionized component of the gas than by the neutral component.

To generalize Emslie's (1978, 1981) treatment to an atmosphere with a *non-uniform* ionized fraction, we first note that the expression (2.9) is fairly insensitive to the ionization dependent quantity β . We therefore assume a value of $\beta = 2$, appropriate for a fully ionized plasma; this approximation makes at most a 25% error in the heating rate in equation (2.9). Second, we note that if $\beta = 2$, the electron stopping depth equations (24) in Emslie (1978) can still be integrated even if the ionized fraction varies with depth. The resulting expression for the heating rate in that case can be written

$$Q(N) = \frac{K \gamma(N) (\delta - 2)}{2\mu_0} B_{x_c} [\delta/2, 1/3] \frac{F_{20}}{E_c^2} \left(\frac{N^*(N)}{N_c^*} \right)^{-\delta/2}, \quad (2.10)$$

where N_c^* is the stopping depth of cutoff energy electrons in a fully ionized plasma (*i.e.* assuming $x = 1$ and $\gamma = \Lambda$), and $N^*(N)$ is the "equivalent ionized column depth" defined as $N^*(N) = \int_0^N \gamma(N')/\Lambda dN'$. The factor of $\gamma(N)$ in equation (2.10) accounts for the local reduction in the heating rate because of the presence of the neutrals, and $N^*(N)$ accounts for the integrated effects of the overlying ionization structure on the local energetic electron distribution. For the sake of simplicity, we assume that the initial pitch angle μ_0 of the energetic electrons is unity in equation (2.10). Picking a different value of μ_0 will only make modest changes to the flare heating distribution with column depth, with smaller values of μ_0 tending to concentrate the flare heating higher in the atmosphere.

Finally, in addition to heating the plasma, non-thermal electrons also contribute an extra collisional ionization term to the statistical equilibrium equations for hydrogen. We adopt the treatment of § IIc of RC to estimate this effect, which includes collisional ionization not only from the primary energetic electrons, but also from secondary electrons excited by the beam.

2.2.2 The Equilibrium Coronal Column Depth

Given a fixed electron spectrum and energy flux, an indefinite period of beam heating will ultimately result in an equilibrium atmosphere with a certain coronal temperature and density structure. We now describe our method for calculating the coronal column depth of an equilibrium, beam-heated atmosphere.

Given a column depth N_{tr} of coronal plasma measured from the loop apex, the flux F_{cor} of energy stopped above that depth may be found by integrating equation (2.10) from 0 to N_{tr} resulting in (Fisher 1989)

$$F_{cor} = \left(1 - \frac{1}{3} B_{x_0}(\delta/2, 1/3) [N_{tr}/N_c]^{1-\delta/2} - (1-x_0)^{1/3}\right) F_{20}, \quad (2.11)$$

where $x_0 = \min(N_{tr}/N_c, 1)$, and where we have taken advantage of the fact that the corona is fully ionized. On the other hand, a static coronal loop of length L which is heated uniformly at level Q_o has a total deposited coronal energy flux of $F_{cor} = Q_o L$. Because previous detailed calculations (cf. Craig, McClymont and Underwood 1978) have shown that global properties of coronal loops are relatively insensitive to where in the loop the energy is deposited, we assume that the uniformly heated loop model having the same energy flux as that deposited by the beam will also have the same coronal column depth.

The heating rate and coronal apex temperature in equilibrium coronal loops are related by (HF92):

$$Q_o = \frac{7}{4} \left(\frac{\beta_1}{2-\alpha}\right)^2 \frac{\kappa_0 T_A^{7/2}}{L^2} \quad (2.12)$$

where $\beta_1 = B[(11/4 - \alpha/2)/(2 - \alpha), 1/2]$, T_A is the apex temperature, $\kappa_0 \simeq 10^{-6}$ (cgs units) is the Spitzer coefficient, and $\alpha = -1/2$ is the approximate coronal cooling rate power law index. Using the equation of state and the static loop scaling law relations

(Craig, McClymont and Underwood 1978; Rosner, Tucker and Vaiana 1978) we can then express the coronal heating flux entirely in terms of the coronal column depth:

$$Q_o L = \frac{7}{4} \left(\frac{\beta_1}{2 - \alpha} \right)^2 \frac{\kappa_0}{L^2} \left(\frac{2k_b \beta_1}{C \beta_2} \right)^{14/(7-2\alpha)} N_{tr}^{14/(7-2\alpha)}, \quad (2.13)$$

where $\beta_2 = B[(7/4 - \alpha/2)/(2 - \alpha), 1/2]$, and $C \simeq 4.25 \times 10^{-10}$ (in cgs units) is the constant appearing in the loop scaling law $PL = CT_A^{11/4 - \alpha/2}$ and is given in equation (5) of HF92 in terms of the various physical constants. Equating the right hand sides of equations (2.13) and (2.11), we find a single transcendental equation for the coronal column depth N_{tr} given a value of F_{20} , which can be easily solved numerically. The quantity N_{tr} found in this manner, together with the loop length L , completely determine the equilibrium coronal loop model consistent with the given level of non-thermal electron energy flux.

2.3 The Pre-Flare Atmosphere

We use the semi-empirical atmospheric model of Metcalf (1991) to approximate the preflare atmosphere in our calculations. Metcalf's model is based on the F1 model of Machado et al. (1980) but with increased density in the upper atmosphere, required to match his MgI observations. Although the Machado F1 model was a weak flare model, Metcalf found that it reproduced well the pre-flare conditions in an active region. Since flares are likely to occur in regions with such initial conditions, we have chosen to use it for our own pre-flare model.

From the pre-flare model we obtain the "quiescent" heating rate necessary to maintain the atmosphere in steady state, by equating the heating with the computed cooling from the atmosphere. We assume this heating comes from internal processes and that it does not change during the external flare heating event. The quiescent heating rate per particle is therefore kept fixed in all the flare models.

In order to make the model complete within our self-consistent framework, we attach a static corona with an apex temperature $T_A \sim 2 \times 10^6 K$ and pressure $P \sim 3 \text{ dyne cm}^{-2}$. The resulting transition region column depth is then $N_{tr} \sim 6.9 \times 10^{18} \text{ cm}^{-2}$. These values set the boundary conditions within which the impulsive models are computed, and act as the starting point from which flare heating and chromospheric evaporation occur in the evolving and equilibrium models.

We caution that recent flare observations (e.g. Canfield *et al.* 1990) indicate that in some cases the pre-flare coronal pressures and densities may be considerably higher than those assumed in our pre-flare model. This may result in some discrepancies between our results and those obtained assuming a denser pre-flare corona, for flares with low heating fluxes.

3. THE MODEL ATMOSPHERES

Here we present in detail our models of the flaring atmospheres. As previously noted, these models are divided into 3 categories, the “Impulsive”, “Equilibrium”, and “Evolving” sets of models. In the Impulsive models (§3.1), the depth of the transition region and the chromospheric hydrogen density structure remain frozen at their pre-flare levels, while the temperature is allowed to change in order to establish a balance between heating by energetic electrons and radiative cooling. These models are intended to approximate conditions early during an impulsive burst of heating, before there has been any significant evaporation. The assumption of energy balance is justified by the extremely short cooling time scale of the heated chromospheric plasma. In order for these models to be valid, the electron energy flux must not exceed the threshold for “explosive” evaporation (Fisher 1987). The Equilibrium models (§3.2) are computed in the opposite limit in which a given level of beam heating is maintained indefinitely. The

depth of the flare transition region (equivalently, the coronal column depth) is determined using the energy balance procedure described in §2.2.2, while in the chromosphere and photosphere the conditions of energetic and hydrostatic equilibrium are imposed. The Evolving models have a transition region depth which depends on the history of flare heating within the loop; the details of this are described further in §3.3. Energetic and hydrostatic equilibrium are imposed in the photosphere and chromosphere. Table 1 summarizes the various assumptions in the models. In the impulsive and equilibrium models, the free parameter is the non-thermal electron energy flux F_{20} ; the evolving models were chosen at three times of particular interest during the evolution of the postulated flare heating profile (see §3.3) and can also be parameterized by F_{20} . Table 2 gives the final model parameters; the apex to footpoint loop length L and loop cross-sectional diameter d are fixed at 10^9 cm and 3.0×10^8 cm, respectively, for all of the atmospheric models. Again, recall that all the parameters are calculated self-consistently under the model assumptions and the condition of energy balance in each part of the atmosphere, once the electron energy flux (in the Impulsive and Equilibrium models) or the time-dependent coronal flare energy flux (in the Evolving models) has been prescribed. The pre-flare model parameters are included for comparison.

3.1 The Impulsive Models

Figure 2 shows (a) the temperature and (b) the electron density as a function of the column mass in the Impulsive chromospheric models, computed for energy fluxes F_{20} of 5×10^8 erg cm⁻² s⁻¹, 5×10^9 erg cm⁻² s⁻¹, and 5×10^{10} erg cm⁻² s⁻¹. The dashed line corresponds to the preflare atmosphere; the vertical line at low column mass indicates the position of the transition region in these models. The transition region has been fixed at its preflare value of $N_{tr} = 6.9 \times 10^{18}$ cm⁻². The stopping depth of a cutoff energy electron ($E_c = 20$ keV) is $N_c = 3.7 \times 10^{19}$ cm⁻² (see §2.2.1). It is clear that

the beam energy deposition peaks at this depth (corresponding to $\log m = -4.2$); the temperature spike in each atmosphere coincides with the heating spike at $N = N_c$. The dominant loss mechanism at the high chromospheric temperatures seen in these models is the optically thin “metal” losses (from all ions not treated by us in detail) described briefly in §2 and in more detail in HF92. Although the temperature peaks are nearly coincident in the three different impulsive models, the depth where the peak electron density occurs does vary with the initial beam flux. The higher beam flux produces residual heating deeper in the atmosphere, increasing the partial ionization of hydrogen significantly at those depths.

Because we do not include backwarming of the lower atmosphere due to the optically thin “metal” radiation, we do not see much heating in the lower chromosphere in these models. However, we expect that this backwarming will result in significant heating deeper in the atmosphere when we include it in the models. This improvement will be incorporated in a future generation of model calculations.

3.2 The Equilibrium Models

Electron energy fluxes F_{20} for the equilibrium models range from a minimum of $5 \times 10^8 \text{ erg cm}^{-2} \text{ s}^{-1}$ to a maximum of $5 \times 10^{10} \text{ erg cm}^{-2} \text{ s}^{-1}$, resulting in coronal emission measures (both halves of the loop included) ranging from $10^{47.5} \text{ cm}^{-3}$ to $10^{49.9} \text{ cm}^{-3}$. It is important to realize that the equilibrium models represent the limiting case of extremely long duration flare heating; most observed episodes of flare heating are not sufficiently long-lived to yield an “equilibrium” atmosphere, especially at the higher energy flux values. Because of this limiting behavior, the results of these models are extremely interesting as they indicate bounds for the expected behavior of various observable radiative diagnostics.

In order to isolate the different mechanisms responsible for heating the flare chromosphere in the equilibrium models, we have computed the temperature structure for each electron energy flux assuming 1) X-ray heating from the overlying corona only, and 2) both X-ray and collisional beam heating. Figures 3(a,b) and 4(a,b) show the respective temperature and electron density structures for the two cases. The dashed lines represent the pre-flare atmosphere, and the vertical lines at the left of the plot indicate the positions of the flare transition region, computed via the procedure of §2.2.2.

One of the most interesting properties of the equilibrium models is that regardless of the input energy flux, the total flux of non-thermal electrons which actually reaches the flare chromosphere and heats it directly is always quite small (see Table 3). Note that because the flare transition region column depth is much greater than the cutoff energy stopping depth ($N_c \sim 3.7 \times 10^{19} \text{ cm}^{-2}$), nearly all of the beam energy is expended in heating the corona. The first model (E1) has sufficiently little beam heating (or X-ray heating for that matter) that the quiescent heating rate still has an appreciable effect on the structure near the top of the chromosphere. Interestingly, as the total energy flux is increased in models E2 and E3, the greater transition region column depths and higher coronal pressures increase the electron density near the top of the chromosphere sufficiently to increase the cooling rate more rapidly than the heating rate. Thus, near the top of the E2 and E3 atmospheres the temperature at the same column depth is even lower than that of the E1 model. Not until the flare energy flux is increased to substantial values (as in the E4 and E5 models) does the chromospheric heating rate increase enough to cause the temperature at fixed N to exceed the other three equilibrium models. At the higher energy flux values, the chromospheric heating rate is dominated by X-rays from the beam-heated corona. Comparing the X-ray only and X-ray plus beam models, we find that collisional beam heating contributes

about half of the flare heating in the E1 model but the contribution falls to essentially none of the heating in the E5 model. In the equilibrium models, then, the beam heats mainly the corona (especially true for strong beams) and X-ray irradiation is the most important chromospheric heating source.

3.3 The Evolving Models

In FH90, we developed a technique for computing the approximate evolution of flaring coronal loops on time scales which are long compared to the loop hydrodynamic time scale ($\tau \sim L/c_s \sim 1$ minute for $L \sim 10^9$ cm). Although this limits the relevance of our technique to flares with fairly long heating time scales, there are numerous examples of flares for which it should be applicable, and where the heating time scale is still far shorter than that necessary to yield an equilibrium model atmosphere.

The coronal evolution model in FH90 is based on integrating the loop energy equation from the base of the loop to the apex, subject to assumptions of a uniform (but time varying) coronal pressure. We derived from this integration an ordinary differential equation for the coronal column depth as a function of time, $N_{tr}(t)$, given a time history of the loop-averaged coronal heating rate $\langle Q(t) \rangle$. Solutions of this equation also give estimates of the coronal temperature, pressure, and emission measure as functions of time. Our “Evolving” models of the flare chromosphere are found by first computing via FH90 the coronal evolution as a function of time for a chosen flare heating rate $\langle Q(t) \rangle$. At selected times during the flare evolution, we then find the non-thermal electron energy flux F_{20} which is consistent with the level of heating $\langle Q(t) \rangle$ at the selected times, using equations (2.11) and (2.13) and the values for the coronal column depth obtained from the coronal evolution model.

Once the coronal column depth and pressure, plus the total energy flux F_{20} have been determined, we compute the structure of the flare chromosphere by imposing energetic and hydrostatic equilibrium. Flare heating in the chromosphere is computed from both collisional beam heating and from heating by X-rays from the overlying corona. Unlike the equilibrium coronal models, however, the coronal temperature structure in the evolving models can deviate significantly from the static coronal loop model of the same column depth described in §2.1; in particular the coronal apex temperature could be significantly hotter or cooler than that of the static model of the same column depth. Such differences in the maximum temperature affect the *spectrum* of the emitted X-rays, but the total coronal radiative output remains nearly invariant (see §III of FH90). To account for such spectral differences in an approximate fashion, we first find the average coronal temperature T_c from the FH90 model ($T_c = PL/[2k_b N_{tr}(1 + (1 + \bar{z})/2)]$, where N_{tr} and P are the coronal column depth and pressure, respectively). Next, we assume that the apex temperature T_A of the loop is given by $T_A = 1.284T_c$, consistent with a temperature variation with depth of a static loop with $\alpha = -1/2$ (see §IV of FH90). Then, the spectrum of the X-ray flux over the 7 wavelength bands is computed from a static loop with this apex temperature using the formalism of §2.1, but the flux at each λ is corrected by multiplying it by the ratio of the total estimated cooling rate of the evolving loop (cf. equation 13 of FH90) to that of the static loop with the same value of T_A .

Our intention in constructing the evolving models is to compute flaring atmospheres that are closer to what one should expect in a real flare than either the impulsive or equilibrium models. We selected for a trial flare heating rate the $\langle Q(t) \rangle$ light curve shown in Figure 5(a) (inspired by the large solar flare reported in Antonucci, Gabriel and Dennis [1984]); the duration of heating, coronal heating amplitude, and time variability are all plausible for a large hypothetical solar flare occurring in a loop

of cross-sectional diameter $d = 3 \times 10^8$ cm and $L = 10^9$ cm. Figure 5(a) also shows the variation of coronal column depth (N_{tr}) with time, while Figures 5 (b,c) show the time variation of the pressure P , the coronal emission measure (computed from both halves of the loop) $EM \simeq (\pi/2)d^2 N_{tr}^2/L$, and the two measures of temperature; T_c , the average coronal temperature, and T_A the “equivalent static loop” temperature (see FH90 for discussion). We computed the three evolving chromospheric models using the procedures described above at the times T1 = 185s, T2 = 240s, and T3 = 690s, coinciding with times of (1) rapidly increasing flare heating, (2) peak flare heating, and (3) maximum pressure and emission measure achieved in the coronal loop.

The model parameters obtained from the loop evolution calculation at these three times are listed in Table 2, and the chromospheric temperature and electron density structures are presented in Figures 6(a,b). While P rises monotonically with time through the 3 models, T_c and N_{tr} become flat and the beam flux F_{20} (which follows Q) goes through a maximum at T2 and drops at T3. The chromospheric models that result from these evolving coronal conditions give us insight into the changing chromospheric response to flare heating within a single loop.

In the T1 model, the column depth of the transition region is again smaller than the stopping depth of the 20 keV electrons, so there is a pronounced peak in the temperature structure where the majority of beam heating is produced in the chromosphere. Note that even with this level of heating, the electron density in the hot chromospheric material is comparable to that at much lower temperature in the deeper but cooler T2 model. The T2 model has the largest energy flux of the 3 models, but less of the beam is deposited in the chromosphere resulting in a less pronounced chromospheric temperature rise. The T3 model chromosphere is barely heated above the quiescent model because of the large overlying pressure. In sum, as the flare loop evolves and the corona becomes hotter and denser, it becomes increasingly difficult for the beam to heat

effectively (as was the case in the equilibrium models). For a beam of this strength (and this is a very strong flare) the resultant coronal heating is not sufficient to produce an effective X-ray heating source; hence the chromosphere experiences very little heating during the later stages of flare evolution.

4. RESULTS

In order to compare our results with observations of the solar atmosphere during flares, we have compiled in Table 3 the relevant chromospheric properties of the models, including the total beam and X-ray fluxes deposited in the chromosphere (and hence acting as heating agents) and the total losses from the chromosphere in metals, hydrogen continuum radiation, all computed emission lines, and, for comparison, the individual losses from $H\alpha$ and Ca II K. The negative values of the hydrogen continuum and the total line radiation in the pre-flare model indicate that those are net *heating* sources in the pre-flare atmosphere. The pre-flare fluxes have been subtracted in each case from the flare models, so that the net effect of the flare heating is revealed. These subtractions are intrinsically noisy if flare induced changes are small compared to the background radiation fields, as is the case for the continuum in all of the models in this paper. To reduce the effects of this noise, values of F_{cont} in Table 3 are obtained by integrating only as deep as flare effects are seen, which coincides roughly with the temperature minimum region (TMR), at a log column mass between -1 and -0.5 depending on the model (see Figure 2-4, and 6). The uncertainty in determining the exact location of the TMR and the discrete spacing of the depth grid still contribute some uncertainty to the values listed. Therefore, although energy balance would demand that the heating sources balance the cooling sources in Table 3 for each model, there are discrepancies at the level of a few times $10^8 \text{ erg cm}^{-2} \text{ sec}^{-1}$. These are insignificant compared to the total continuum flux of a few times $10^{10} \text{ erg cm}^{-2} \text{ sec}^{-1}$.

Several trends are immediately evident from Table 3. In the impulsive models, the portion of the beam flux deposited in the chromosphere increases monotonically with the total beam flux F_{20} , which is expected since nearly all of the beam energy is being deposited in the chromosphere (see Section 3.1). All of the loss rates have a similar monotonic rise, with the losses from “metals” becoming increasingly important, and dominating in the I5 model. The equilibrium models, in contrast, show a nearly constant value of the beam flux deposited in the chromosphere, despite a two order of magnitude increase in F_{20} . For instance, the E5 model experiences only about 50% more chromospheric heating from the beam than does the E1 model. The X-ray flux, on the other hand, rises dramatically, becoming the dominant heating source in the E4 and E5 models. The reason is simple: virtually all of the beam is being stopped in the corona and very little is available to heat the lower atmosphere. Raising the beam flux, at least to these levels (levels which are consistent with observation, and which do not result in explosive evaporation) increases the amount of *coronal* heating, and hence, through evaporation, increases the coronal pressure, temperature and conductive flux, acting to compress the chromosphere and to prevent significant chromospheric beam heating. The resulting hot, dense corona does emit more X-radiation however, which accounts for the increase in X-ray heating of the chromosphere.

The cooling rates from the metals, hydrogen continuum and total line radiation rise nearly in tandem by an order of magnitude from the E1 model to the E5 model, in response to increased X-ray heating, while $H\alpha$ increases only by \sim a factor of 2. We discuss $H\alpha$ line formation in more detail in Section 4.1 below. The X-ray heated only equilibrium models confirm that X-ray irradiation is the only important heating source in our models at high beam fluxes, since the E4 and E5 models (with beam heating) are very similar to the corresponding E4X and E5X models (without beam heating). Finally, the evolving models show a monotonic decline in total heating (though the X-ray

contribution increases from 0.1% in the T1 model to 50% in the T3 model) accompanied by decreases in all of the cooling rates as the flare evolves. However, the cooling does *not* follow the beam flux (F_{20}) which reaches a peak in model T2 and declines in model T3.

In §4.1 we examine the important optical flare diagnostic $H\alpha$ in more detail, including a comparison with previous models. In §4.2 we compare our model results with recent simultaneous X-ray and $H\alpha$ observations.

4.1 $H\alpha$ Results

The $H\alpha$ flux profiles computed from our impulsive, equilibrium and evolving models are shown in Figure 7 (a,b,c) respectively. The brightest, broadest profiles are found in the most energetic impulsive model (I5) and the earliest evolving model (T1), i.e. in those models with relatively low coronal pressure but large electron flux, and hence significant chromospheric heating from the beam. Note that the evolving models are marked by a decrease in both the strength and width of $H\alpha$ as the flare evolves. The equilibrium models show relatively little $H\alpha$ emission even in the most energetic beam case (E5); again this is the result of the large overlying pressure and conductive flux which drives the transition region (TR) to great depth and effectively eliminates chromospheric heating from the beam. However, the impulsive models, though showing broader profiles than seen in the evolving models, have less $H\alpha$ flux - even though the I5 model has a factor of 10 greater chromospheric heating from the beam than does the T1 model. In fact, Figure 8 shows that the correlation of $H\alpha$ flux with chromospheric heating is different for each set of models, with the impulsive models having relatively less $H\alpha$ flux per unit of heat input *into the chromosphere* than the equilibrium or evolving models, and the evolving models showing the greatest $H\alpha$ response. Clearly it is not just the amount of heating but the specific response of each atmosphere to the

heating that determines the H α behavior (we discuss the details of the line formation in terms of the line source functions for each set of models in section 4.1.2 below).

To examine the central reversal in the line profiles, we compute the quantity

$$\chi_{cen} = \frac{F(\text{line center})}{F(\text{line peak})} \quad (4.1)$$

where χ_{cen} approaches zero for an infinitely dark absorption line and unity for an unreversed emission line. Figure 9 shows χ_{cen} as a function of $\log F_{20}$ for each set of models. All points fall in a narrow band increasing (i.e. the profiles are less reversed) toward higher F_{20} . When we plot χ_{cen} vs. pressure, there is good correlation only for models where F_{20} and P are themselves correlated (the evolving and equilibrium models). Thus, it appears that F_{20} is the important parameter for determining the depth of the H α central reversal in our models. The solid lines in Figure 9(a) correspond to the simple linear relations

$$\chi_{cen} \pm 0.1 = 0.22 \log F_{20} - 1.47 \quad (4.2)$$

which fits all of the models including the pre-flare (Q1) model. (Note that the EX models are not included as they are not self-consistent, beam heating having been purposely excluded.) We caution that this relation is only an empirical fit to our model results and should not be applied indiscriminately; we discuss the central reversal behavior in terms of the line source functions in §4.1.2 below. However, because χ_{cen} is independent of area (the H α flux, for example, is not), equation 4.2 could potentially be a valuable tool for determining F_{20} from H α data alone.

4.1.1 Comparison with Previous Models

CGR were (to our knowledge) the only previous authors to compute theoretical $H\alpha$ profiles showing the effects of various heating mechanisms in solar flares using static chromospheric models. (See Canfield and Gayley 1987; Gayley 1991; and Gayley and Canfield 1991 for discussion of $H\alpha$ profiles from dynamic models.) The CGR models, most of which were taken from RC, were computed under many of the same assumptions as ours, with the major difference that they used a parametric representation of the corona rather than a self-consistent energy balance description as we have done. They considered the impulsive and equilibrium limits (as have we) and from the profiles they computed, obtained the following results:

Impulsive Models:

- (1) Large electron flux (F_{20}) reduced the central reversal.
- (2) Large conductive flux reduced the width and intensity of $H\alpha$ profile;

Equilibrium Models:

- (1) Large electron flux (F_{20}) led to wide, bright $H\alpha$ profile with a deep central reversal;
- (2) Large conductive flux reduced width and intensity of $H\alpha$ profile;
- (3) Large pressure led to dramatic increase in width and intensity of $H\alpha$ profile, with no central reversal.

Because CGR described the corona parametrically, the electron flux (F_{20}), the conductive flux and the coronal pressure were allowed to vary independently. In our self-consistent energy balance scheme, the impulsive models are assumed to be bounded by the pre-flare corona (which is not allowed to vary). The equilibrium models result

from an electron flux which evaporates the upper chromosphere, increasing the coronal pressure and temperature, driving a larger conductive flux into the chromosphere which results in a deeper transition region. Hence the electron flux, conductive flux and coronal pressure are all intimately connected, and many of the parameter combinations in the CGR models are not physically permitted. We find that in both our impulsive and equilibrium models a large electron flux reduces the central reversal, in agreement with CGR's impulsive result, but in conflict with their equilibrium result. Further, in the equilibrium models, the very bright $H\alpha$ intensity and broad Stark wings seen in the CGR high pressure models are not reproduced in our models, because high pressure is naturally accompanied by a large conductive flux which counteracts this effect. That is, the CGR high pressure models actually have the transition region further out (at lower column mass) than the low pressure models, while the increased conductive flux acts to move the transition region further in (to deeper layers, higher column mass). When we include both effects in our more physically consistent fashion, we find that high pressure and high conductive flux occur in tandem, and always lead to a deep transition region and hence reduced chromospheric heating.

4.1.2 $H\alpha$ Line Formation

We find from our numerical solutions to the rate and transfer equations that, in general, the shape of the computed $H\alpha$ flux profile can be understood in terms of the Eddington-Barbier relation (in this discussion we ignore the distinction between flux and specific intensity): $F(\Delta\nu) \simeq S_l(\tau_{\Delta\nu} = 1)$, where S_l is the line source function, $\Delta\nu$ measures frequency shift away from line center, and $\tau_{\Delta\nu}$ is the corresponding frequency dependent optical depth. Given that result, understanding the shape of the $H\alpha$ profile is tantamount to understanding the depth dependence of the source function since, as

the radiation frequency moves away from line center, the point at which optical depth unity occurs moves increasingly deeper into the atmosphere.

MULTI assumes that $H\alpha$ is formed in complete redistribution, so the line source function is frequency independent and is proportional to the ratio of populations between levels 3 and 2 of the H atom. The level populations are determined directly through collisional and radiative rates between levels 2 and 3, and indirectly through rates between levels 2 and 3 and the other levels. The qualitative behavior of the source function with depth in our model atmospheres can be understood by ignoring the indirect rates and considering a balance between the direct rates: $n_2 C_{23} = n_3 C_{32} + n_3 A_{32} \rho_{32}$, where C_{23} and C_{32} are the collisional rate coefficients for excitation and de-excitation respectively, A_{32} is the Einstein coefficient for spontaneous radiative de-excitation, and $\rho_{32} \equiv 1 - \bar{J}/S_l$ is known as the “escape coefficient” (Athay 1972), or the “flux divergence coefficient” (Canfield and Puetter 1981). The quantity \bar{J} appearing in the definition of ρ_{32} is the frequency averaged mean intensity in the line. The above rate equation results in $S_l \propto C_{23}/(C_{32} + A_{32}\rho_{32})$. Over most of the line-forming region of the atmosphere, the $H\alpha$ source function has de-thermalized (the source function has fallen below the Planck function), and C_{32} is small compared with $A_{32}\rho_{32}$, meaning that for most of the atmosphere, $S_l \propto C_{23}/(A_{32}\rho_{32})$. In many circumstances, ρ_{32} depends only on line center optical depth, as for example is the case when ρ_{32} is approximated by the “single flight escape probability” (see *e.g.* Rybicki 1984). We shall assume this is the case in our discussion below. In general, $|\rho_{32}|$ is small at large values of line center optical depth τ_{23} , and approaches 1/2 as $\tau_{23} \rightarrow 0$. At a fixed value of τ_{23} we can then write

$$\log S_l \approx \log N_e + (1/2) \log T - \frac{2.2 \times 10^4}{\ln(10) T} + C, \quad 4.3$$

where we have made use of the general temperature and electron density dependence of the collisional excitation rate $C_{23} \propto N_e T^{1/2} \exp(-T_{ex}/T)$, $T_{ex} \approx 2.2 \times 10^4$ K is

the temperature corresponding to the $H\alpha$ line excitation energy, and the constant C includes atomic constants and $-\log \rho_{32}$. With equation 4.3 we can relate differences in the line source function at a given line center optical depth to differences in T and N_e in the individual atmospheres.

In Figure 10 we present the line source function S_l computed by MULTI, together with the temperature and electron density as a function of $H\alpha$ line center optical depth for four of our models. The 4 models chosen for the comparison are the T1, I5, E5, and E1 models shown in panels a-d, respectively. Each of the 4 panels uses the same scales for S_l , T , and N_e , so the results are directly comparable.

We consider three aspects of the profile: the central reversal, the line wings, and the overall flux level.

(1) Central Reversal: The central reversal in the $H\alpha$ profile is usually explained by the increase in ρ_{32} as $\tau_{23} \rightarrow 1$; i.e. substantial numbers of $H\alpha$ (line center) photons are able to escape the atmosphere when it becomes optically thin, resulting in a decrease in the line source function. In the equilibrium models we find that the decrease in S_l is compounded by the decrease in N_e at $\tau_{23} \sim 1$. The “dips” in the electron density are quite noticeable at the top of the chromosphere in each of the equilibrium models in Figure 4, and correspond to the shallow dips seen at $\log \tau \sim 0$ in the E1 and E5 panels of Figure 10 (which are on a compressed scale). The N_e dips occur where the Lyman continuum radiation field becomes optically thin, hence allowing Lyman continuum photons to escape and removing an important radiative ionization rate which then reduces N_e . These N_e dips were also seen by RC in their models.

Assuming that ρ_{32} depends only on τ_{23} , the differences in the central reversal between the different equilibrium models can therefore be explained by the differences in amplitude of the density dips seen in Figure 4. Examining Figure 4 leads to the conclusion that the central reversal will be large for the E1 model and small for the E5

model; Figure 7b and Figure 8 confirm that this is the case. The decrease in amplitude of the N_e dip in the equilibrium models as F_{20} is increased occurs because high values of F_{20} lead to high pressure, and hence the collisional ionization rates are relatively more important than the radiative rates in determining the electron density.

It is interesting to note that the profile for the E5 model (Figure 7b) shows a small bump at line center, not seen in any of the other line profiles. This bump results from emission from the optically thin part of the atmosphere. Figure 10c shows that S_l becomes very large at small optical depths owing to the large values of N_e (in turn a result of the very large overlying pressure in the E5 model). This represents a counterexample to our general finding that features in the line profiles can be explained in terms of the Eddington-Barbier approximation.

The impulsive models also show a decrease in the amplitude of the central reversal as F_{20} is increased (see Figure 7a). The origins for this can be determined by examining Figure 2, comparing the temperature and electron density in the three models. Both T and N_e increase as F_{20} increases, resulting in source functions which increase as a function of F_{20} at fixed τ_{23} (note also that the impulsive models generally have higher values of the source function than those of the equilibrium models; compare *e.g.* the S_l curves between the E5 and I5 models in Figure 10). More importantly, because the chromospheric temperature in these models is sufficiently high that hydrogen is fully ionized above the penetration depth of the cutoff-energy electrons, collisional rates are relatively more important at the top of these atmospheres as compared to radiative rates as F_{20} is increased, to the extent that the source function is coupled more effectively to the Planck function. The source function therefore does not drop as steeply around $\tau_{23} \sim 1$, and thus the central reversal is smaller in the atmospheres with larger F_{20} .

The amplitude of the central reversal as measured by the quantity χ_{cen} is nearly the same for all three evolving models, as shown in Figure 9. The T1 model in Figure 10a has roughly constant N_e in the central line forming region, and relatively high temperature due to chromospheric beam heating. Thus the source function is elevated (compared to *e.g.* most of the equilibrium models) at optical depths around $\tau_{23} = 1$, and also shows a moderate slope at this optical depth. This results in a bright profile overall, and an intermediate value of the central reversal. Figure 6 shows that the electron density does not change significantly between the T1, T2, or T3 models, but that the region with elevated temperature at the top of the atmosphere disappears due to the increase in the coronal column depth which stops the beam electrons from reaching the chromosphere. Further, the density dip seen in the equilibrium models is also observed in these evolving models, becoming more pronounced in the atmospheres with higher overlying pressure. The result of this combination of effects is that the profiles become less bright overall, but the amplitude of the central reversal stays roughly constant.

In summary, the equilibrium atmospheres, with increasingly greater coronal pressure and hence chromospheric electron density at roughly the same temperature show progressively smaller central reversals, with the E5 model being almost entirely filled in. The impulsive atmospheres, with relatively lower electron density but increasingly higher temperature due to greater chromospheric beam heating also have progressively smaller central reversals due to increasing contributions from the hot, ionized gas. The evolving models, due to a combination of density and temperature, all have central reversals of intermediate value.

2) Line Wings: Our models are computed with complete frequency redistribution, so we caution that comments on the line wings are only suggestive. Our version of MULTI computes line broadening in $H\alpha$ from radiation damping, Van der Waals broadening, and Stark broadening. The Stark damping rate is due to the electric field of neighboring

electrons, and is proportional to $N_e^{2/3}$, where N_e is the ambient electron density. Stark broadening is incorporated using “method 2” of Sutton (1978), in which an effective damping rate is derived which can be added to the radiative and Van der Waals rates. Sutton (1978) demonstrates that this method introduces an insignificant error in the overall computed spectral line shape. The overall wavelength dependence of the line emissivity is then assumed to be a Voigt profile (see *e.g.* Mihalas 1978) with the combined damping coefficient from all the above mechanisms. In our flaring atmospheres, Stark broadening is usually the most important broadening mechanism. At a fixed frequency in the line wings (much further from line center than a Doppler width), the emissivity due to Stark broadening is proportional to $N_e^{2/3} T^{1/2}$.

The E5 model has the highest N_e of any of the models shown in Figure 10, but because of its low temperature it has less emission in the wings (see Figure 7) than the T1 and I5 models, which show the greatest wing emission. The E1 model has both low electron density and low temperature at depth, and in fact it has virtually no wing emission. Thus emission in the wings of $H\alpha$ in our models indicates an increase in both the temperature and electron density at significant depths in the chromosphere, and therefore seems to be an indicator of deep chromospheric heating (as, for example, by the beam). This conclusion regarding wing emission is similar to that reached by CGR.

3) Overall Flux Level: In the atmospheric models shown in Figure 10, the total flux can be easily understood in terms of the electron density and temperature which determine the overall level of the source function. The T1 model with relatively high density and temperature has the greatest flux; the I5 model with lower density but higher temperature also has a relatively large total flux, while the E5 model with high density but low temperature has a relatively small flux. Temperature appears to be somewhat more important than density in determining the overall flux level, but it is the combination of relatively high temperature (*i.e.* $> 10,000K$) with elevated electron density that

gives the greatest flux. In the hottest impulsive models, the temperature is so high that most of the hydrogen is ionized and thus the $H\alpha$ flux is reduced below what might have been expected. Therefore it is not just chromospheric heating that leads directly to $H\alpha$, but heating in a certain part of the atmosphere, and in the correct amount to produce the proper temperature and density conditions, that gives rise to large $H\alpha$ fluxes. This is illustrated clearly in Figure 8, which shows that the same total heating flux can yield significantly different $H\alpha$ fluxes, depending on how the energy is deposited in the chromosphere.

Finally, it is important to note that in our models, the atmospheres never received the kind of chromospheric heating necessary to produce the very broad, unreversed $H\alpha$ profiles at large flux levels that are actually observed in flares.

4.2 Comparison to Observations

Canfield, Zarro, Wülser and Dennis (1991) (hereafter CZWD) measured the ratio $F_{H\alpha}/F_{20}$ as a function of time during flares (F_{20} being found from hard X-ray observations) with the result that the ratio obeyed a power law distribution in F_{20} ,

$$\frac{F_{H\alpha}}{F_{20}} \propto F_{20}^{-0.7 \pm 0.1} \quad 4.4$$

for their sample of 5 flares. That is, the $H\alpha$ flux decreases relative to the beam flux as the beam flux increases. They compared this observational result with the CGR models and found that they could fit the $H\alpha$ to F_{20} ratio with a double power law in pressure and beam flux, but the pressure exponent changed with F_{20} . In addition, though they use pressure P_5 in their fits, which is the pressure at 10^5K found from the pressure – conductive flux relationship, the models on which the results were based are the CGR

models, which had the coronal pressure as a free parameter. The pressure in the fit is therefore not necessarily consistent with that used to generate the model.

In our equilibrium and evolving models, the pressure, conductive flux *and beam flux* are physically related, so that we have only one free parameter – the beam flux F_{20} . In the impulsive models, the pressure and beam flux are decoupled, and the pre-flare pressure is fixed, so again F_{20} is the only free parameter. In Figure 11(a), we plot $\log F_{H\alpha}/F_{20}$ as a function of $\log F_{20}$ for the impulsive, equilibrium and evolving models. Also shown is a line with the observed slope of -0.7, and with the vertical adjusted so that the ratio has roughly the observed values at the F_{20} limits 10^8 and 10^{11} . The impulsive models follow a well-defined power law with slope of -0.57, which is close to the observed value, while the amplitude of the ratio is about an order of magnitude below that observed. (Amplitude effects can be explained, as in CZWD, by invoking a filling factor which describes the area difference between the beam emitting area and the $H\alpha$ emitting area.) The equilibrium models at low beam flux have a steeper dependence, which flattens at high beam flux because X-ray heating of the lower atmosphere becomes important. The evolving models, which (we hoped) were designed to simulate a real flare evolution, scatter over the plot and show no obvious dependence of the ratio on the beam flux.

Because we found that the amount of beam heating (with the caveat that it needed to be in the right place) was the important factor in determining the $H\alpha$ flux, and because the amount of chromospheric heating is controlled by the overlying coronal pressure, we show in Figure 11(b) $\log F_{H\alpha}$ as a function of $\log P$ for our models. We also show the observed data for four of the five flares analyzed by CZWD (and kindly provided to us by them). The direction of flare evolution is indicated with arrows for the observations. Although there is no longer an obvious power law dependence, the evolving models now appear to follow more closely the observed behavior. We suggest

that the physically relevant parameter in describing chromospheric emission *from a single loop* after the initial impulsive phase is the pressure and not the beam flux F_{20} . However, the relationship between $F_{H\alpha}$ and P is a complex one, reflecting the discussion surrounding Figure 8 with regard to the changing $H\alpha$ response to differing amounts and depths of chromospheric heating.

5. SUMMARY and SPECULATION

We have constructed models of the solar flare atmosphere for the limiting cases of impulsive and equilibrium conditions, and for a set of intermediate, evolving states. The models use a static, one-dimensional plane parallel geometry and are designed within a physically self-consistent coronal loop in energy balance from photosphere to coronal apex. We have computed the chromospheric radiation, particularly in the widely observed diagnostic $H\alpha$, that results from a range of coronal heating rates by a flux of non-thermal electrons. We find that:

- (1) Only in the impulsive models, and the earliest evolving model where the coronal pressure is still low (i.e. in models where little evaporation has occurred) does the non-thermal electron flux provide significant heating in the chromosphere. In the impulsive models, however, more than 95% of the beam energy is deposited in the chromosphere.
- (2) In the equilibrium models, and the later evolving models (after evaporation has occurred), the dominant source of chromospheric heating is the X-ray irradiation from the hot corona. However, this reprocessed heat source never exceeds about 6% of the original flare energy flux deposited in the corona by the beam.
- (3) In order to obtain the broad, intense $H\alpha$ profiles that are actually observed in flares, there must be either (a) a condition of low coronal pressure as in the impulsive models, or the evolving models before significant evaporation occurs; or (b) heating at

the top of the chromosphere from a source other than the beam and its products (X-rays, heat conduction). The reason is that only with a low pressure corona is there enough chromospheric heating from the beam to raise enough column mass to temperatures of $\sim 10^4\text{K}$ necessary to produce copious $H\alpha$. Under a high pressure corona the beam energy is deposited in the corona and the X-rays never become a sufficiently strong source to provide the needed heat input.

(4) The depth of the $H\alpha$ central reversal was correlated with the incident coronal beam flux F_{20} in our models in the sense that models with large beam flux have profiles with smaller central reversal. We can explain this correlation by examining the detailed temperature and density structures of the model atmospheres and their effects on the line source function.

(5) The “metal” losses play a very important, and in many cases dominant, role in the cooling of the chromosphere. It is essential that future modelling efforts both treat these losses more rigorously, and include the effects of the radiation backwarming on the lower atmosphere. However, the backwarming effects alone are unlikely to produce enough heating to provide the heat source discussed in (3b), above, since F_{metal} is roughly of order F_{X-ray} in most of the models. An exception is the early evolving model where there is significant beam heating of the chromosphere and F_{metal} is much larger than F_{X-ray} .

(6) The power law dependence of the ratio $F_{H\alpha}/F_{20}$ on the beam flux F_{20} seen in the observations of CZWD was similar to that found with the impulsive models and equilibrium models, although the equilibrium models no longer followed a power law dependence once X-ray heating became important in the high beam flux models. The evolving models failed to reproduce any semblance of the observed flare evolution. A more physically meaningful parameter *during the evolution of a single loop* is the pressure, P ,

since the chromospheric heating after evaporation has occurred depends primarily on the coronal pressure (or alternatively the conductive flux or coronal column depth) and not on the beam flux.

Given the results and implications of our models, we engage in the following speculation: With the heating mechanisms and self-consistent description of the atmosphere that we use, the observed $H\alpha$ can only be produced under conditions of a low pressure corona with strong beam heating. Therefore we suggest that $H\alpha$ in flares is produced primarily at the footpoints of newly heated loops where significant evaporation has not yet occurred. As a single loop evolves in time, no matter how strong the heating rate may become, the $H\alpha$ will decay rapidly as the corona becomes denser and hence more effective at stopping the beam.

This speculation has several observable consequences that could be tested with simultaneous, high spatial and temporal resolution observations of coronal (hard and soft X-ray) and chromospheric ($H\alpha$) radiation from individual flare kernels. In particular, the hard X-rays should initially correlate well with cospatial $H\alpha$ fluxes, but prolonged hard X-ray heating of any magnitude should be accompanied by a decrease in $H\alpha$ flux *at that location*. Meanwhile, as other kernels are subsequently heated (as in, for example, a two ribbon flare), the sites of major $H\alpha$ emission should shift to those kernels. Further, the seeming correlation of *soft* X-ray emission (presumably produced in heated, dense coronal regions) with prolonged $H\alpha$ line emission must be shown to be merely an overlap of X-ray emission from a coronal site with a hot dense loop (but no chromospheric emission) with $H\alpha$ emission from a freshly heated, not yet evaporated loop at another site. We look forward to new X-ray and ground-based observations that could be used to test these predictions.

Acknowledgments

We thank Mats Carlsson for the use of his computer program MULTI, and Dick Canfield, Dominic Zarro and J.-P. Wülser for providing us with unpublished data that we used in our analysis. We thank Dick Canfield and Jeff de la Beaujardiere for useful discussions of the observed properties of $H\alpha$ profiles. SLH was supported by NASA grant NAGW-2547 and NSF grant ATM 90-22385, and also by a Hubble Fellowship through NASA Grant No. HF-1017.01-91A awarded to the Space Telescope Science Institute which is operated by the Association of Universities for Research in Astronomy, Inc., for NASA under Contract No. NAS5-26555. Part of the research was done at the Lawrence Livermore National Laboratory under the auspices of the United States Department of Energy, through Contract No. W-7405-ENG-48. GHF was supported by NASA grants NAGW-2969 and NAGW-3429, and by NSF grant AST-9218085.

References

- Antonucci E., Gabriel A.H. and Dennis B.R. 1984, ApJ, 287, 917
- Auer L., Heasley J. & Milkey R. 1972, *Kitt Peak National Observatory Contribution No. 555*
- Avrett E.H., Machado M.E., & Kurucz R.L. 1986, in *The Lower Atmosphere of Solar Flares*, ed. D.F. Neidig (Sunspot: National Solar Observatory), p. 216
- Brown J.C. 1971, Solar Physics, 18, 489
- Canfield R.C. & Gayley K.G. 1987, ApJ, 322, 999
- Canfield R.C., Gunkler T.A. & Ricchiazzi P.J. 1984, ApJ, 282, 296 (CGR)
- Canfield R.C., McClymont A.N. & Puetter R.C. 1983, in *Methods in Radiative Transfer*, ed. W. Kalkofen (Cambridge: Cambridge University Press)
- Canfield R.C. & Ricchiazzi P.J. 1980, ApJ, 239, 1036
- Canfield R.C., Zarro D.M., Wülser J.P. & Dennis B.R. 1991, ApJ, 367, 671
- Canfield R.C., Zarro D.M., Metcalf T.R. & Lemen J.R. 1990, ApJ, 348, 333
- Carlsson M. 1986, *Uppsala Astronomical Observatory Report No. 33*
- Craig I.J.D., McClymont A.N. & Underwood J.H. 1978, A&A, 70, 1
- Emslie A.G. 1978, ApJ, 224, 241
- Emslie A.G. 1981, ApJ, 245, 711
- Fisher G.H. 1987, ApJ, 317, 502
- Fisher G.H. 1989, ApJ, 346, 1019
- Fisher G.H. & Hawley S.L. 1990, ApJ, 357, 243 (FH90)

- Gan W.Q. & Fang C. 1990, ApJ, 358, 328
- Gayley K. 1990, *Ph.D. Thesis*, University of California at San Diego
- Gayley K.G. 1991, ApJ, 374, 773
- Gayley K.G. & Canfield R.C. 1991, ApJ, 380, 660
- Hawley S.L. and Fisher G.H. 1992, ApJS, 78, 565 (HF92)
- Machado M.E., Avrett E.H., Vernazza J.E. & Noyes R.W. 1980, ApJ, 242, 336
- Mauas P.J.D., Machado M.E. & Avrett E.H. 1990, ApJ, 360, 715
- Metcalf T.R. 1991, *Ph.D. Thesis*, University of California at San Diego
- Metcalf T.R., Canfield R.C. & Saba J.L.R. 1990, ApJ, 365, 391
- Mihalas D. 1978, *Stellar Atmospheres*, Second Edition, (San Francisco:Freeman)
- Raymond J.C., Cox D.P. & Smith B.W. 1976, ApJ, 204, 290
- Raymond J.C. & Smith B.W. 1977, ApJS, 35, 419
- Ricchiazzi P.J. 1982, *Ph.D. Thesis*, University of California at San Diego
- Ricchiazzi P.J. & Canfield R.C. 1983, ApJ, 272, 739 (RC)
- Rosner R., Tucker W.H. & Vaiana G.S. 1978, ApJ, 220, 643
- Scharmer G.B. & Carlsson M. 1985, J. of Comp. Phys., 59, 56

Figure Captions

Figure 1: Schematic diagram of loop geometry used for X-ray irradiation calculations. Symbols are discussed in the text.

Figure 2: (a) log Temperature T (K) vs. log Column Mass m (g cm^{-2}) for the Impulsive models. (b) log Electron Density N_e (cm^{-3}) vs. log m for the Impulsive models.

Figure 3: Same as Figure 2 for the Equilibrium models with X-ray heating only.

Figure 4: Same as Figure 2 for the Equilibrium models with both X-ray and beam heating.

Figure 5: Results of coronal loop evolution model from FH90. All quantities are shown as a function of time (s) during the flare. (a) Flare heating rate $Q(t)$ ($\text{erg cm}^{-3} \text{s}^{-1}$) and log coronal column depth N_{tr} (cm^{-2}); (b) Coronal pressure P (dyne cm^{-2}) and log emission measure EM (cm^{-3}); (c) Average coronal temperature T_c and equivalent apex temperature T_A ; temperatures are in units of 10^7 K.

Figure 6: Same as Figure 2 for the Evolving models.

Figure 7: $\text{H}\alpha$ profiles, flux relative to the continuum vs. wavelength (\AA). (a) Impulsive models; (b) Equilibrium models; (c) Evolving models.

Figure 8: Log $\text{H}\alpha$ flux vs. the level of chromospheric heating from the beam and X-rays, $\log(F_{beam} + F_{X-ray})$. All fluxes are in units of ($\text{erg cm}^{-2} \text{s}^{-1}$).

Figure 9: The $\text{H}\alpha$ central reversal depth χ_{cen} defined in Equation 4.1 vs. the log of the beam flux F_{20} ($\text{erg cm}^{-2} \text{s}^{-1}$).

Figure 10: The log of the $\text{H}\alpha$ line source function S_l ($\text{erg cm}^{-2} \text{s}^{-1} \text{Hz}^{-1}$), log Temperature T (K), and log Electron Density N_e (cm^{-3}) as a function of $\text{H}\alpha$ line center optical depth. The source function scale is shown on the left y-axis in all four panels. The density scale is shown on the right y-axis in panels a) and c) but applies to all four panels. The temperature scale is shown on the right y-axis in panels b) and d), but also applies to all four panels. The four models depicted are: (a) T1; (b) I5; (c) E5; (d) E1.

Figure 11: (a) The log of the ratio $F_{H\alpha}/F_{20}$ vs. the beam flux F_{20} ($\text{erg cm}^{-2} \text{s}^{-1}$). (b) The log of the $H\alpha$ flux, $F_{H\alpha}$ ($\text{erg cm}^{-2} \text{s}^{-1}$) vs. the coronal pressure, P (dyne cm^{-2}). The arrows show the direction of time evolution of the data.

Table 1

Model Assumptions

Models	Stage of Loop Evolution	Corona	Transition Region	Chromosphere	Number of Models
Impulsive I1,I3,I5	Early	pre-flare	pre-flare	beam heated only	3
Equilibrium E1-5	Late	energy equilibrium with beam	pressure equilibrium with corona	beam and x-ray heated	5
E1-5X	Late	energy equilibrium with beam	pressure equilibrium with corona	x-ray heated only	5
Evolving T1,T2,T3	Intermediate	time dependent, from FH model solutions	pressure equilibrium with corona	beam and x-ray heated	3

Table 2

Coronal Properties of Model Atmospheres

Model	F_{20}	Q_{cor}	T_A	P	$\log N_{tr}$	F_{cond}	$\log EM$
Q1	–	0.01	2.0	3.4	18.84	0.2	45.7
I1	0.5	0.01	2.0	3.4	18.84	0.2	45.7
I3	5	0.01	2.0	3.4	18.84	0.2	45.7
I5	50	0.01	2.0	3.4	18.84	0.2	45.7
E1	0.5	0.4	5.7	78	19.75	4.0	47.5
E2	1	0.9	7.2	158	19.95	8.0	47.9
E3	5	4.9	11.7	676	20.37	34	48.8
E4	10	9.9	14.2	1236	20.54	63	49.1
E5	50	49.8	22.7	4953	20.95	250	49.9
T1	6.2	3.9	10.9	105	19.56	5.3	47.3
T2	10	9.1	14.1	335	19.98	17	48.1
T3	4.7	4.7	14.3	809	20.36	41	48.9

F_{20} = total electron beam flux (10^9 erg cm^{-2} sec^{-1})

Q_{cor} = average coronal heating rate (erg cm^{-3} sec^{-1})

T_A = coronal apex temperature (10^6 K)

P = coronal and transition region pressure (dyne cm^{-2})

N_{tr} = column depth at transition region ($T = 2 \times 10^5$ K) (cm^{-2})

F_{cond} = conductive flux at $T = 10^5$ K (10^7 erg cm^{-2} sec^{-1})

EM = emission measure, assuming loop radius = 1.5×10^8 cm (cm^{-6})
(includes both sides of loop)

Table 3
Chromospheric Properties of Model Atmospheres

Model	F_{20}	F_{beam}	F_{x-ray}	F_{metal}	F_{cont}	F_{lines}	$F_{H\alpha}$	F_{CaK}
Q1	—	—	—	0.87	-2.82	-4.25	-10.6	-112
I1	5	4.87	—	1.60	4.63	0.77	3.07	6.61
I3	50	49.2	—	37.5	1.30	2.33	9.15	15.4
I5	500	482	—	451	37.7	5.29	22.6	22.3
E1	5	2.26	0.10	1.04	2.87	0.25	4.34	2.70
E2	10	2.24	0.26	1.56	1.89	0.23	4.02	3.04
E3	50	2.62	1.84	3.10	2.32	0.27	4.24	4.08
E4	100	2.87	4.35	13.5	4.12	0.43	4.99	6.62
E5	500	3.57	30.9	15.6	14.8	1.45	11.0	21.4
E1X	5	—	0.10	0.18	0.62	-0.05	0.61	0.39
E2X	10	—	0.26	0.65	0.68	-0.03	0.83	0.84
E3X	50	—	1.85	2.02	1.22	0.09	1.89	2.65
E4X	100	—	4.35	5.54	2.23	0.24	3.23	4.23
E5X	500	—	30.9	13.4	12.8	1.36	10.2	20.2
T1	62	47.5	0.04	23.1	24.4	2.83	30.7	19.6
T2	100	20.1	0.34	10.7	11.5	1.11	16.6	8.80
T3	47	2.56	1.92	3.45	1.11	0.24	4.35	2.98

F_{20} = total electron beam flux (10^8 erg cm^{-2} sec^{-1})

F_{beam} = electron beam flux deposited in chromosphere (10^8 erg cm^{-2} sec^{-1})

F_{x-ray} = xray flux deposited in chromosphere (10^8 erg cm^{-2} sec^{-1})

F_{metal} = flux from "metals" emitted by chromosphere (10^8 erg cm^{-2} sec^{-1})

F_{cont} = flux in hydrogen continuum emitted by chromosphere (10^8 erg cm^{-2} sec^{-1})

F_{lines} = flux in emission lines emitted by chromosphere (10^8 erg cm^{-2} sec^{-1})

$F_{H\alpha}$ = flux in hydrogen Balmer alpha line emitted by chromosphere (10^6 erg cm^{-2} sec^{-1})

F_{CaK} = flux in Calcium II K line emitted by chromosphere (10^6 erg cm^{-2} sec^{-1})

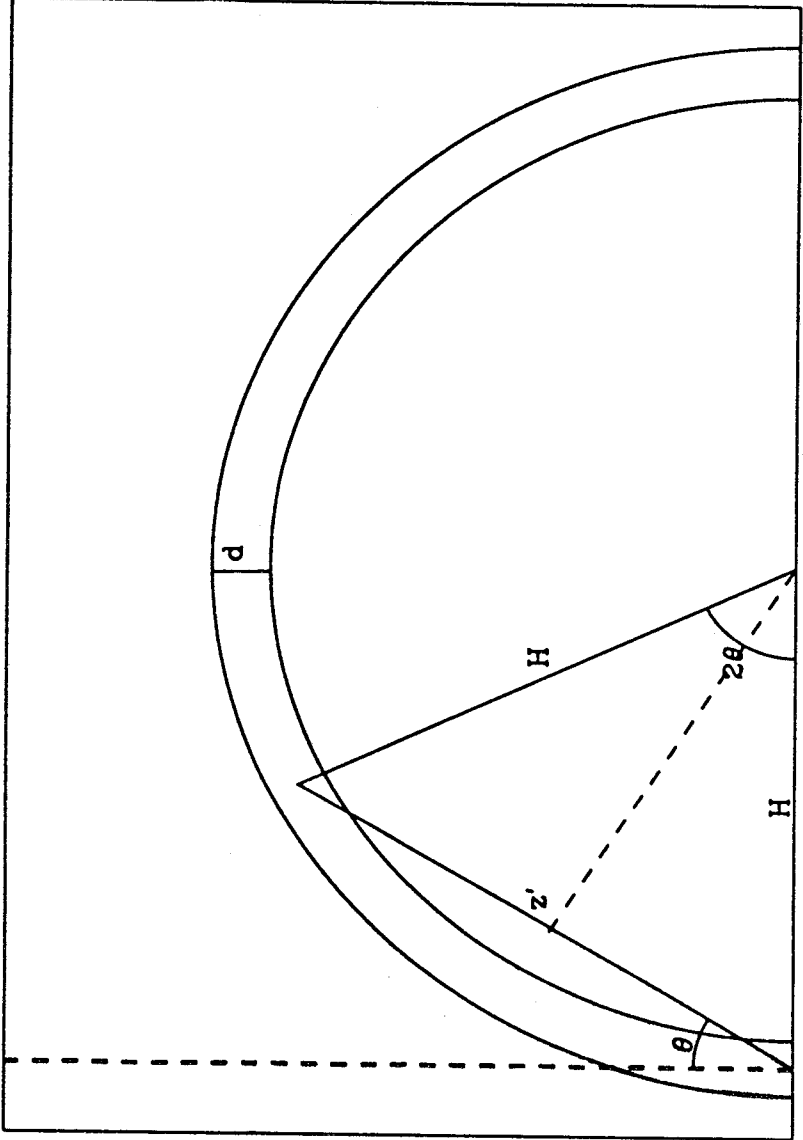


Fig 1

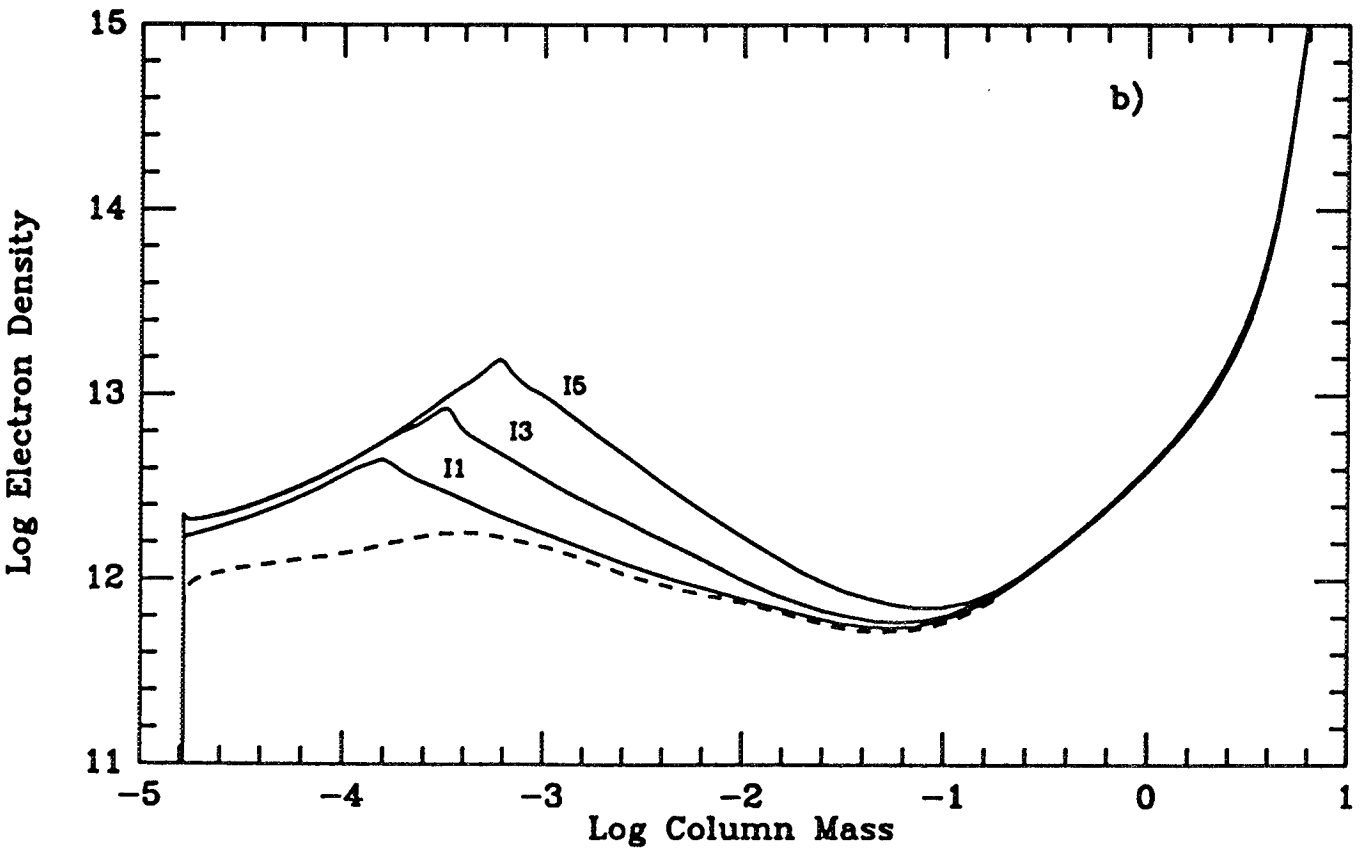
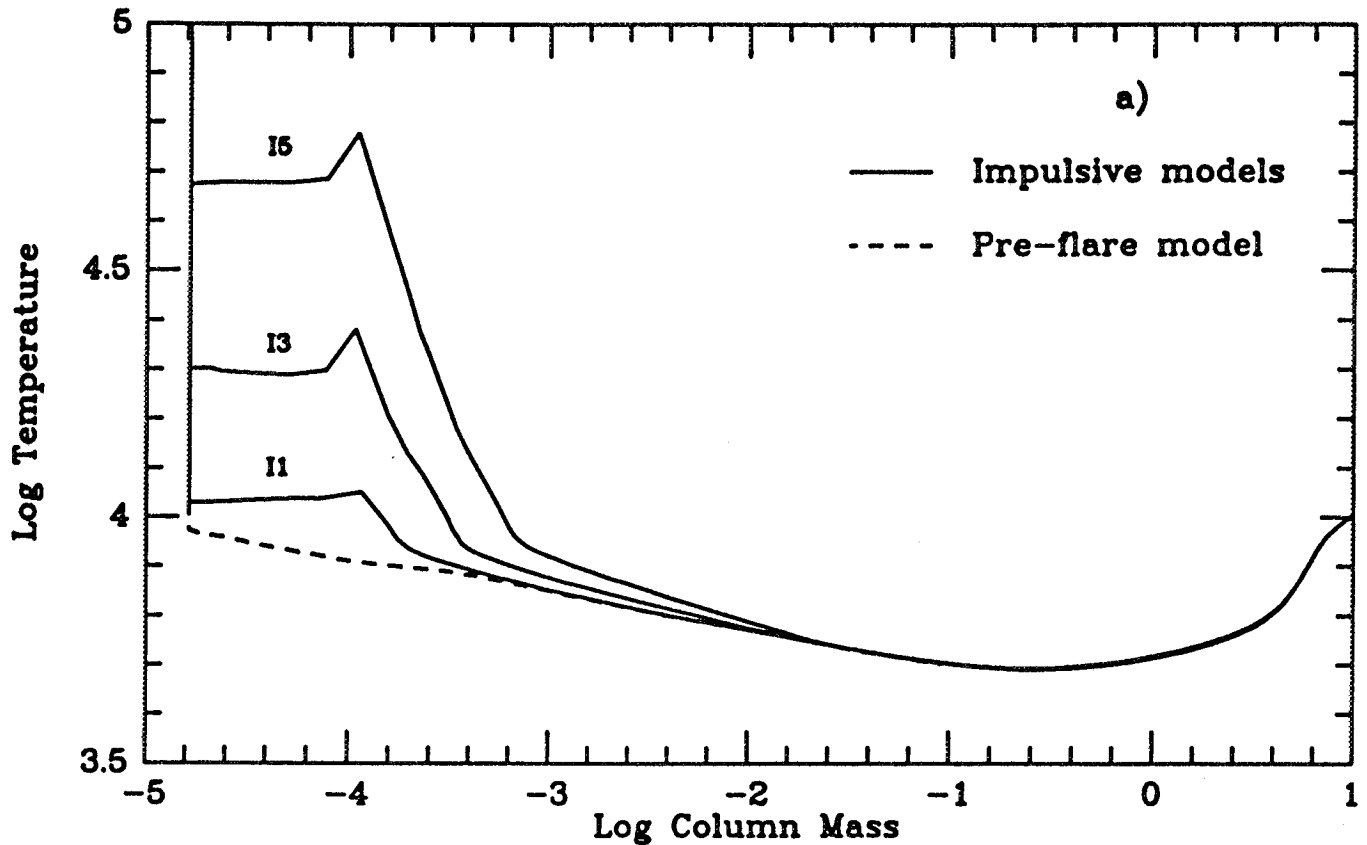


Fig 2

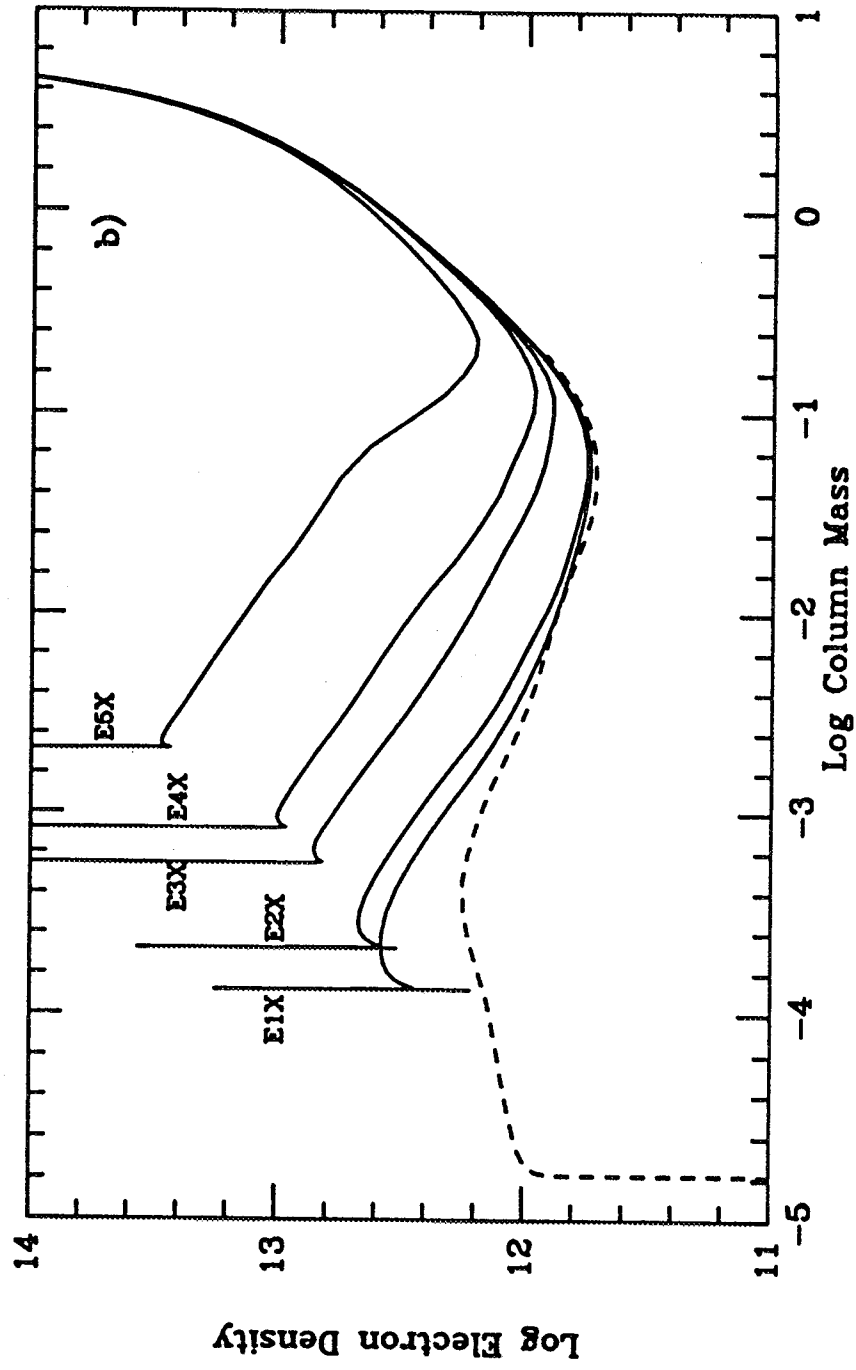
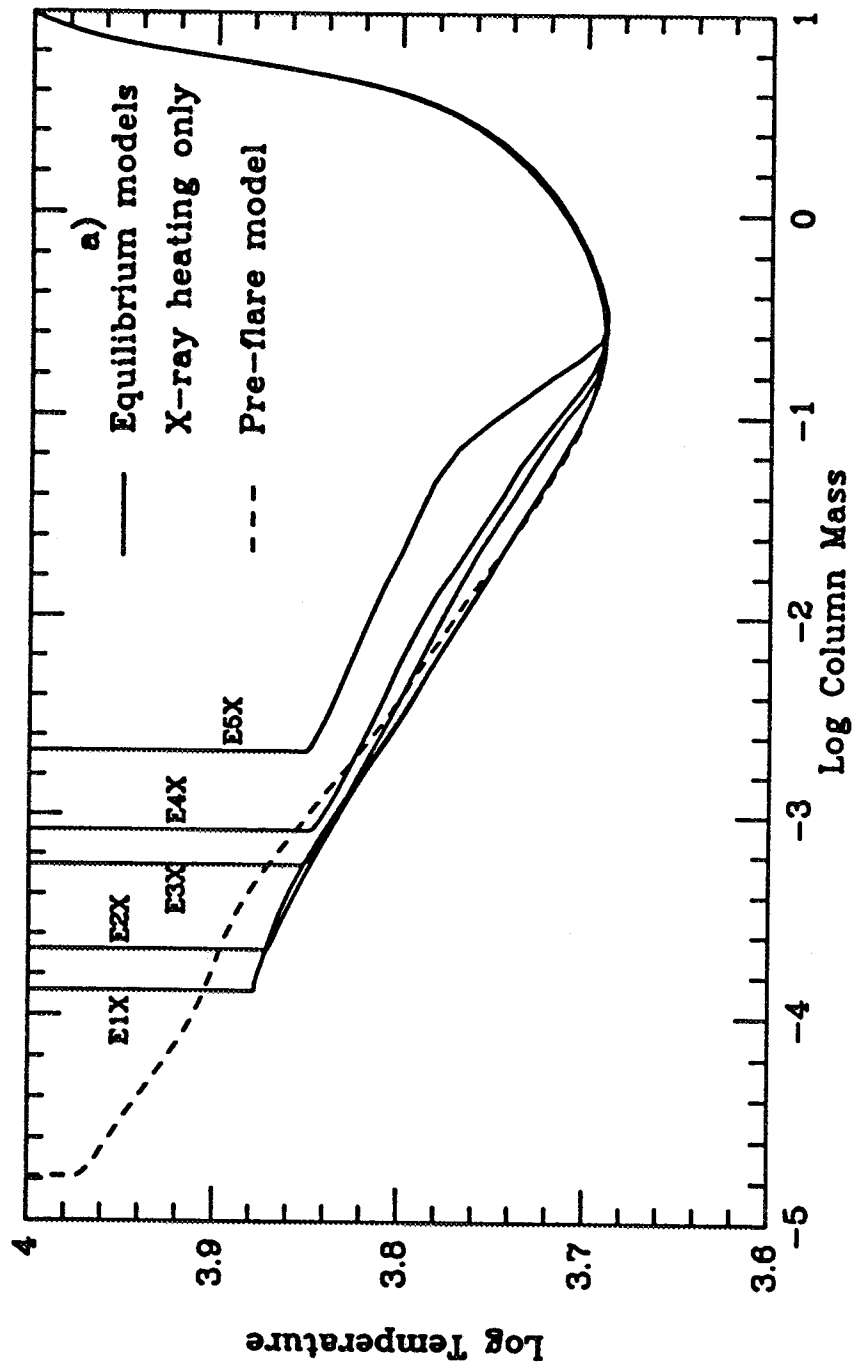


Fig 3

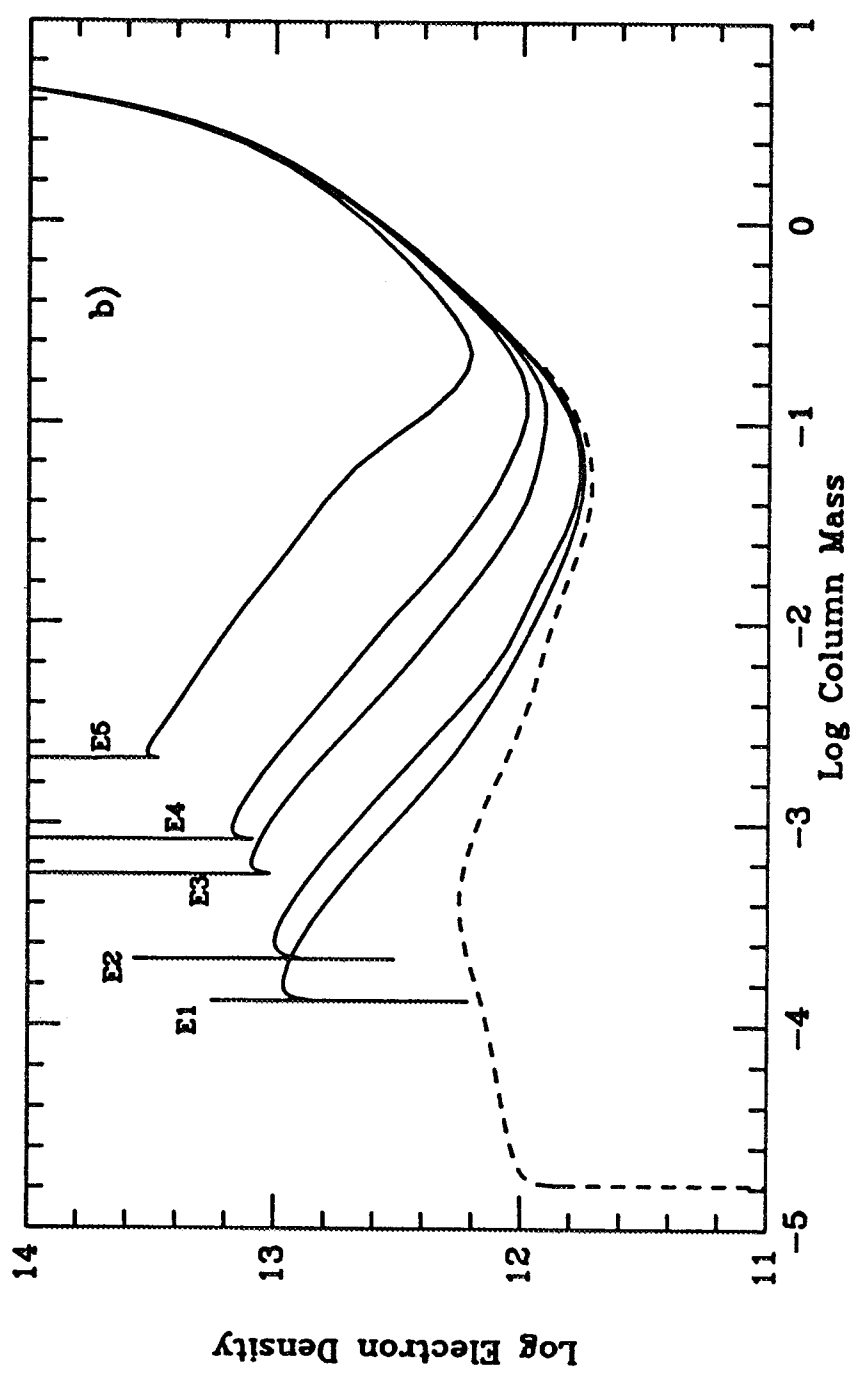
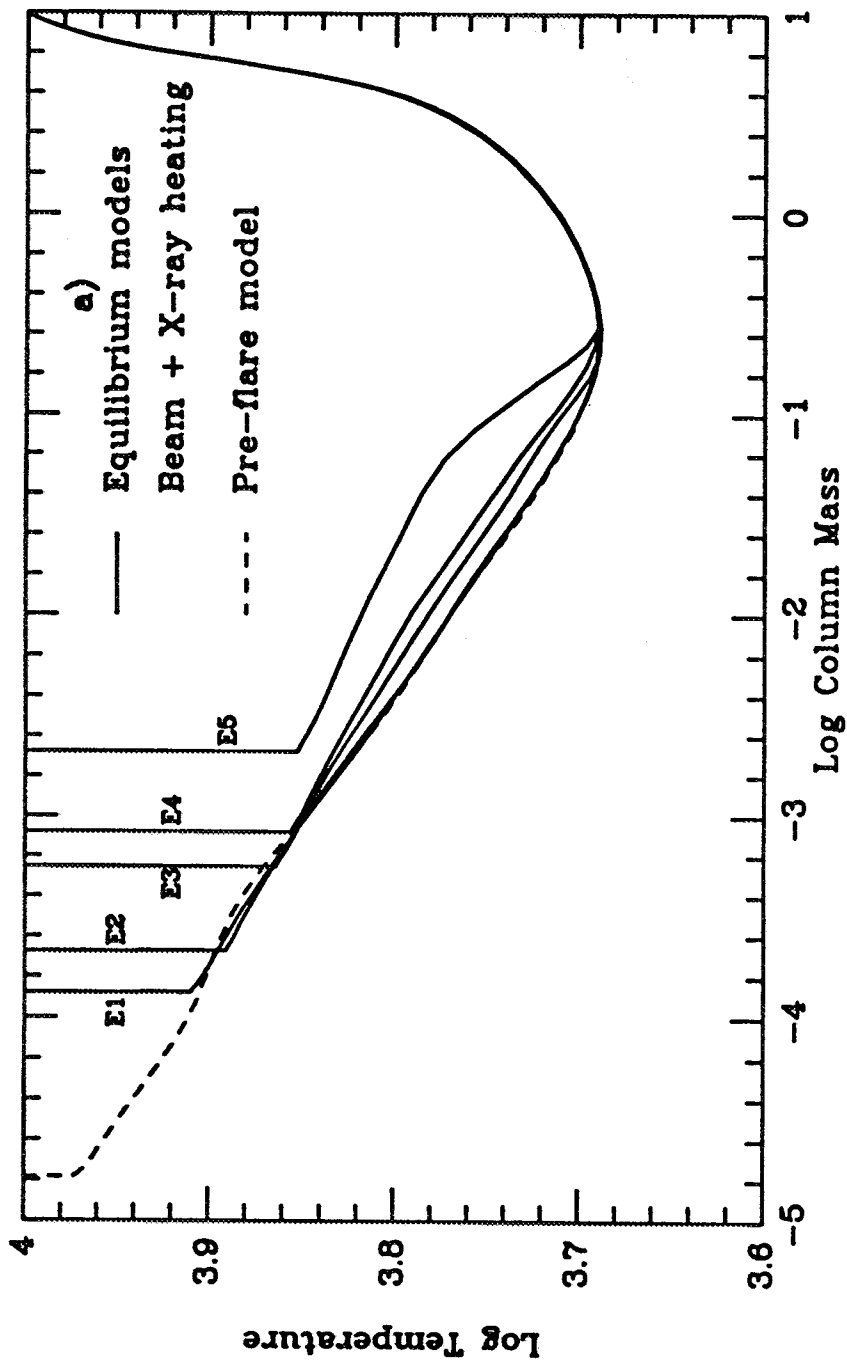


Fig 4

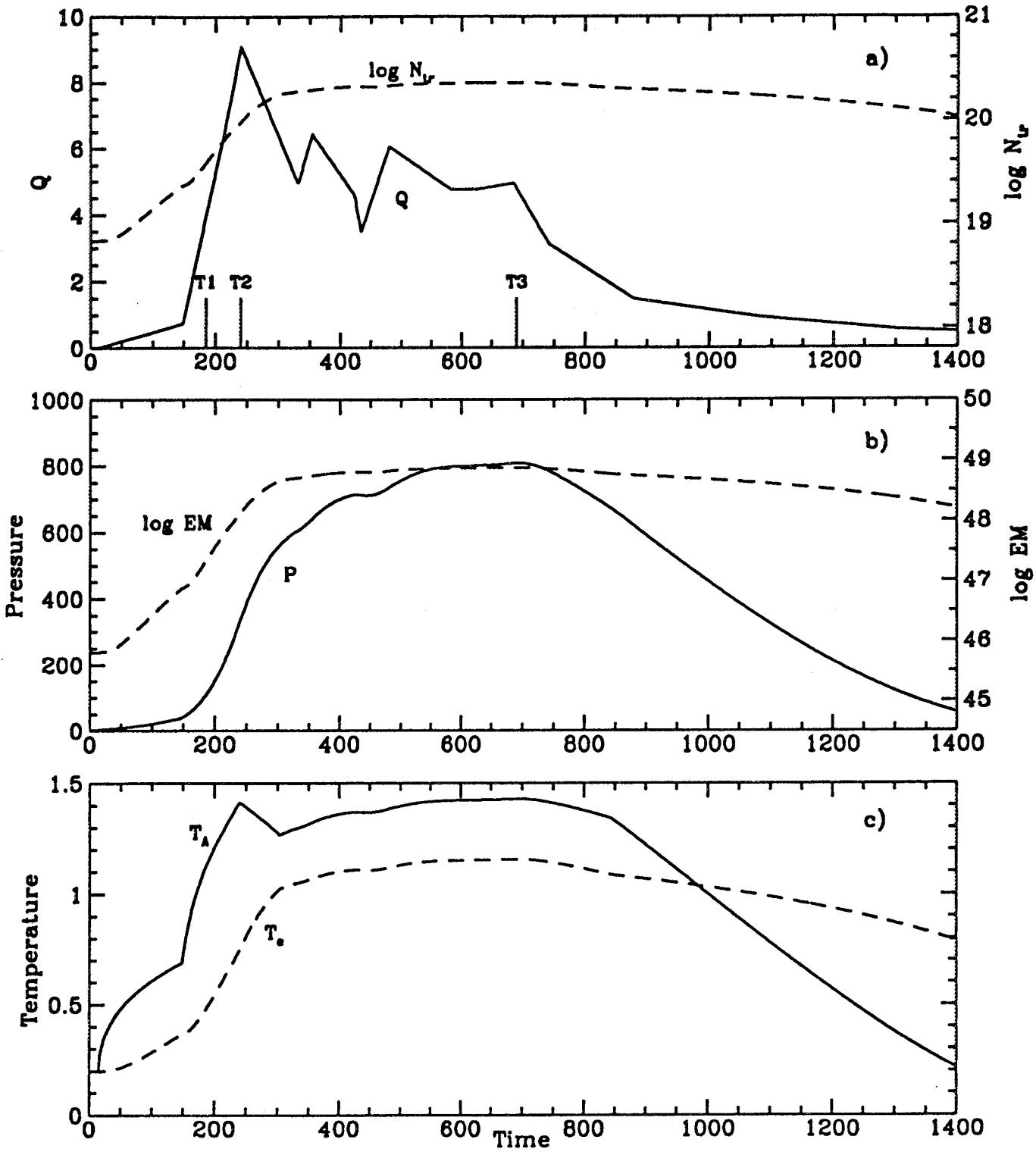


Fig 5

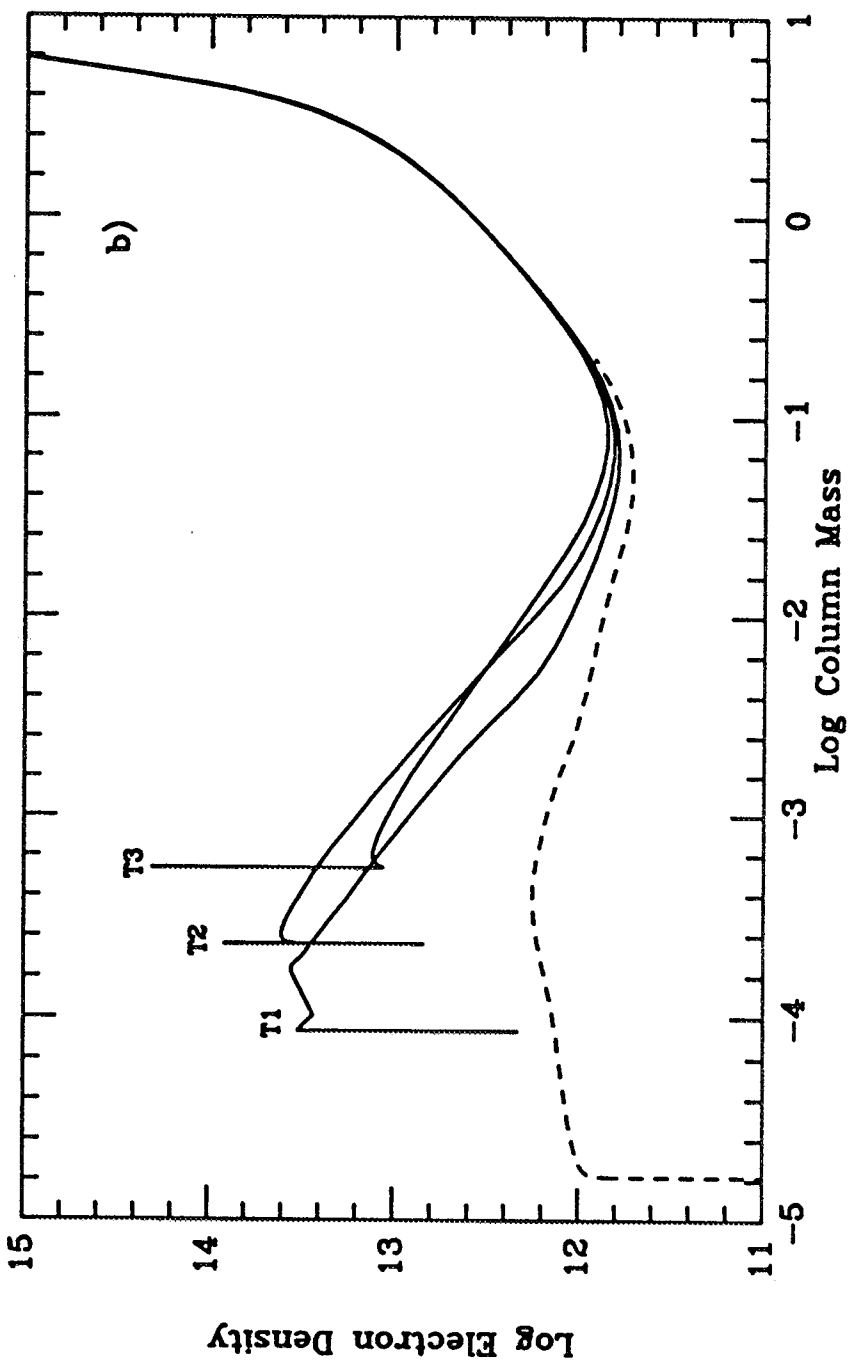
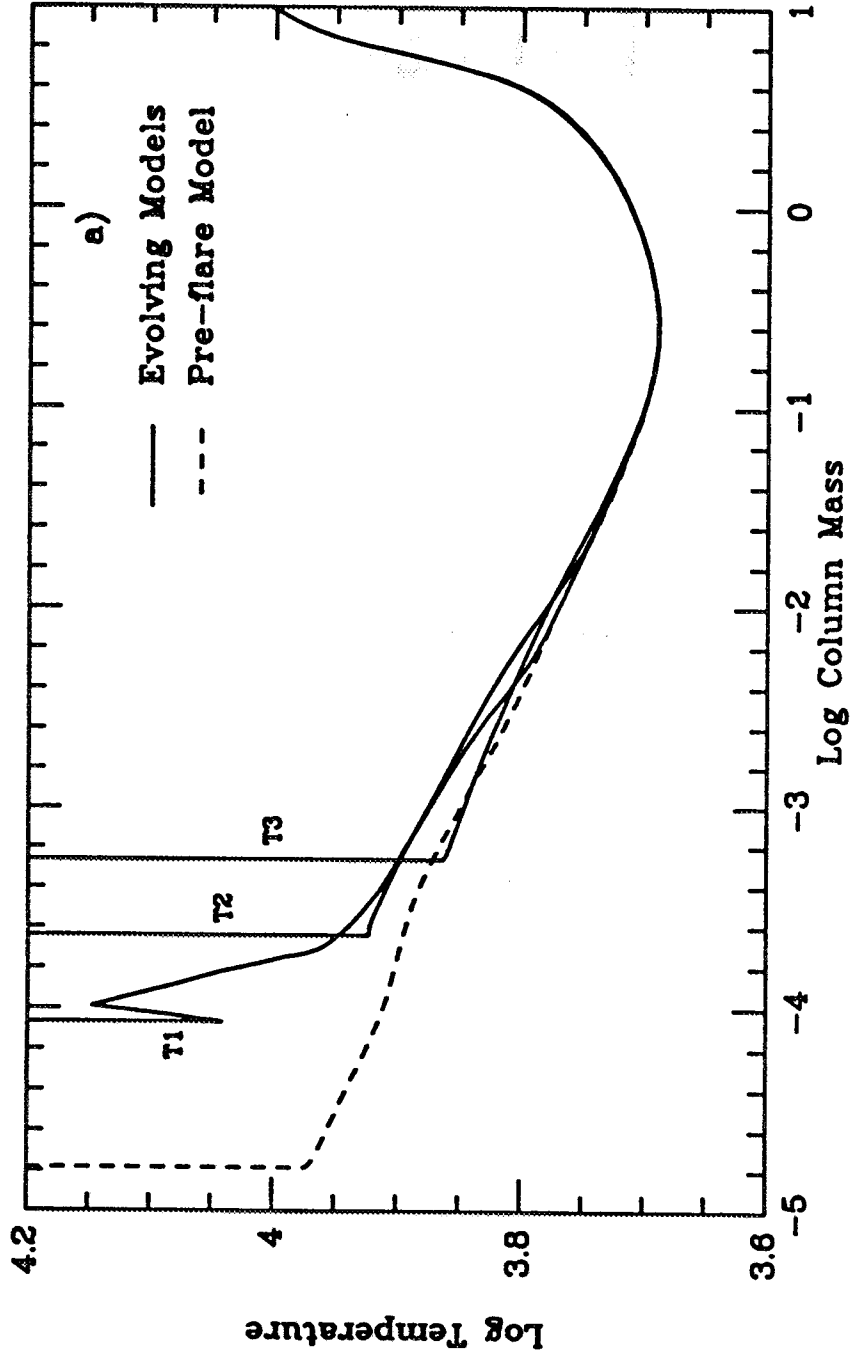


Fig 6

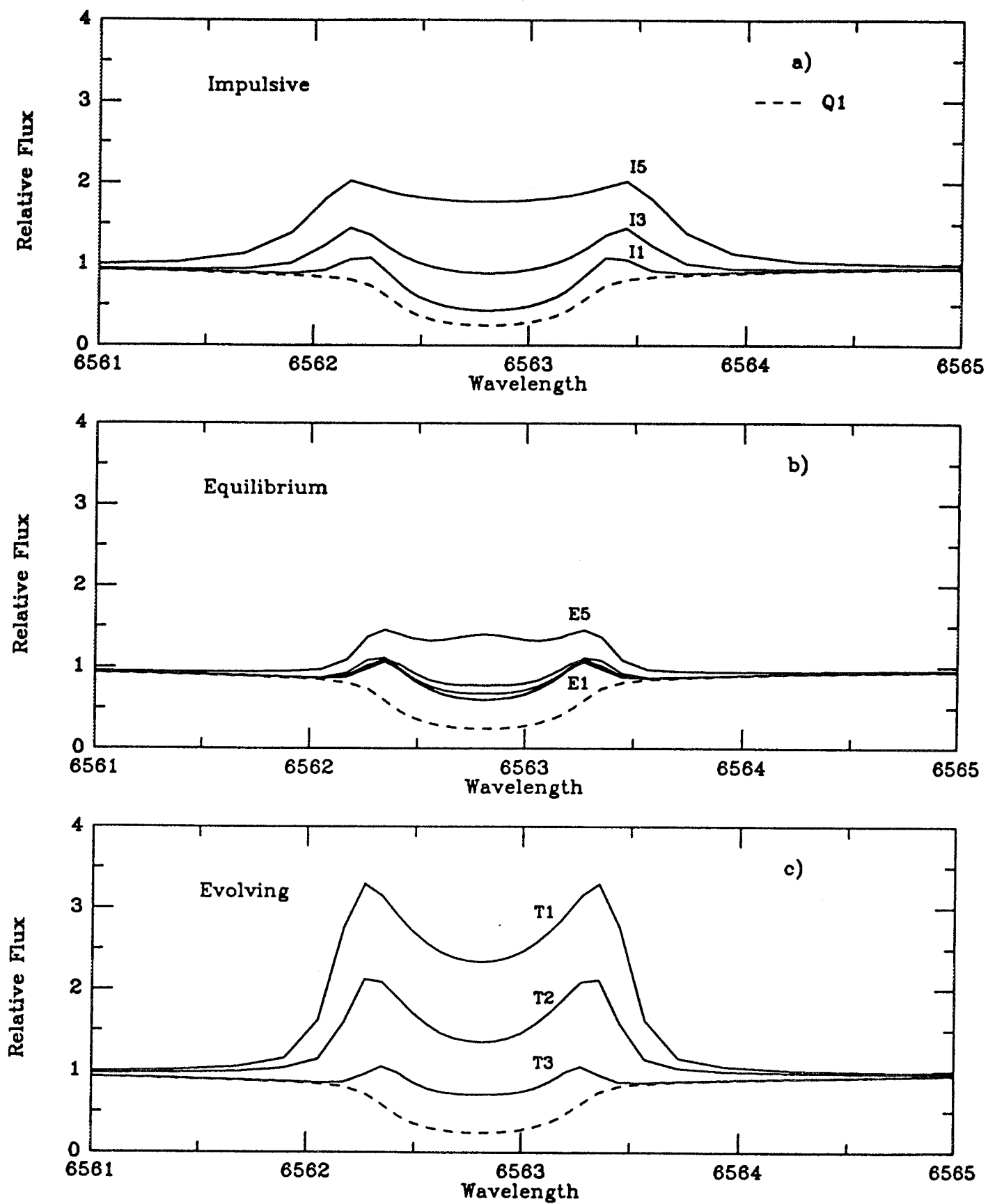


Fig 7

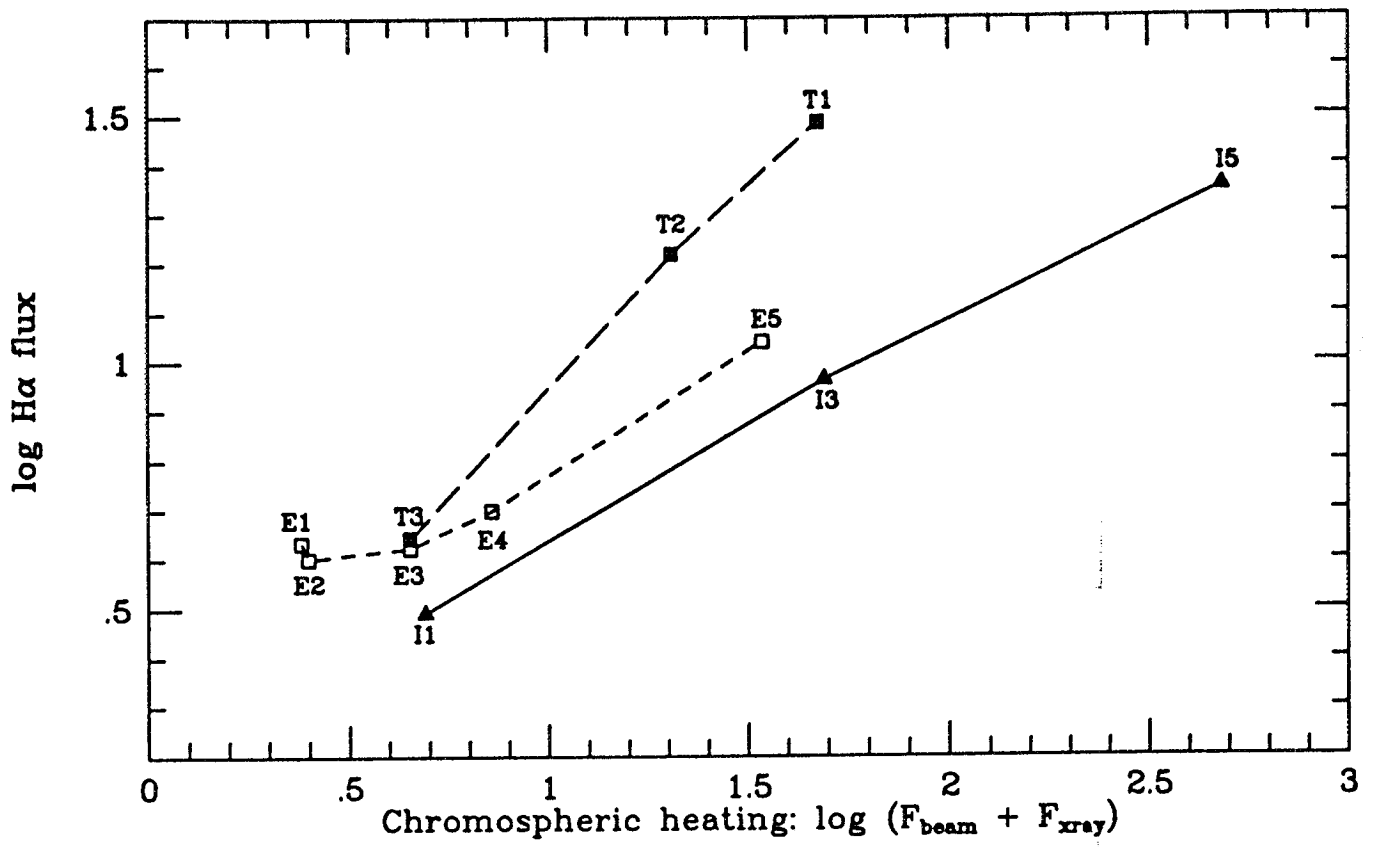


Fig 8

Fig 9

